



## UvA-DARE (Digital Academic Repository)

### Bending benzenes and twisting light

Kovida, K.

**Publication date**  
2026

[Link to publication](#)

#### **Citation for published version (APA):**

Kovida, K. (2026). *Bending benzenes and twisting light*. [Thesis, fully internal, Universiteit van Amsterdam].

#### **General rights**

It is not permitted to download or to forward/distribute the text or part of it without the consent of the author(s) and/or copyright holder(s), other than for strictly personal, individual use, unless the work is under an open content license (like Creative Commons).

#### **Disclaimer/Complaints regulations**

If you believe that digital publication of certain material infringes any of your rights or (privacy) interests, please let the Library know, stating your reasons. In case of a legitimate complaint, the Library will make the material inaccessible and/or remove it from the website. Please Ask the Library: <https://uba.uva.nl/en/contact>, or a letter to: Library of the University of Amsterdam, Secretariat, P.O. Box 19185, 1000 GD Amsterdam, The Netherlands. You will be contacted as soon as possible.

# 5

## How do Nanohoops Exercise Their Strain in [5]Helicene Racemization?

---

This chapter has been published as: Kovida K.; Malinčík J.; Groot T.D.; Šolomek T. How do Nanohoops Exercise Their Strain in [5]Helicene Racemization? *J. Org. Chem.* 2025, 90, 46, 16607–16614.

## Abstract

The effect of strain in curved carbon nanohoops has a major impact on their optoelectronic properties. How this strain affects their dynamics and reactivity is, however, far less documented in the literature. Here, we investigate the effect of strain on racemization of [5]helicene, which we embedded in three different [*m*]cycloparaphenylenes ( $m=5-7$ ). [5]Helicene is a prototypical organic molecule with helical chirality that racemizes at room temperature. We synthesized and separated the enantiomers of the strained helicene-paraphenylene macrocycles, and we investigated their racemization as a function of temperature. Our results revealed that the configurational stability of the [5]helicene increases with increasing nanohoop size, with activation free energies ranging from 25 to 29 kcal mol<sup>-1</sup>. The combination of the experimental data and DFT calculations established a clear relationship between the strain and the racemization in helicene-embedded nanohoops.

## 5.1 Introduction

Helicenes, a class of chiral polycyclic aromatic hydrocarbons with *ortho*-fused phenylenes adopting helical shape, are of great interest in asymmetric catalysis, molecular electronics, and chiral sensing.<sup>1–3</sup> A critical stereodynamic characteristic of [*n*]helicenes is their configurational stability, which directly impacts any chirality-related application of helicenes. Experimental and theoretical studies<sup>4–10</sup> have shown that the racemization mechanism in helicenes varies with the size of the helix. Shorter helicenes ( $n = 4–7$ ) undergo a concerted, single-step inversion, while larger systems ( $n \geq 8$ ) follow a multi-step pathway. The shortest of the helicenes, [4]helicene, is configurationally unstable, but [5]helicene exhibits an activation free energy ( $\Delta G_{\ddagger}^{\ddagger}$ ,  $T = 298\text{K}$ ) of  $24.1 \text{ kcal mol}^{-1}$ ,<sup>11</sup> sufficient for resolution of enantiomers. However, racemization occurs in a matter of days. From [6]helicene onward, the enantiomers remain configurationally stable at room temperature.<sup>9</sup>

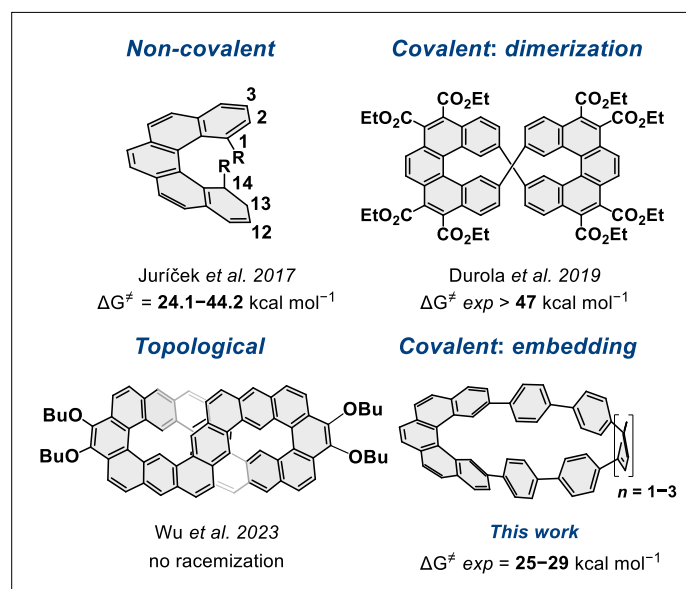


Figure 5.1. Configurational “locking” in [5]helicenes.<sup>8,12,13</sup>

To improve configurational stability of [5]helicene, substituents can be installed to its fjord, noncovalently “locking” the configuration by employing steric hindrance (Figure 5.1). Placement of a single methoxy group improves the  $\Delta G_{423}^{\ddagger}$  to  $32 \text{ kcal mol}^{-1}$ , and increasing the steric bulk with methyl substituents in the 1,14 positions accomplishes the [5]helicene derivative with the configurational stability that matches [9]helicene with  $\Delta G_{503}^{\ddagger} \sim 44 \text{ kcal mol}^{-1}$ .<sup>8</sup> The substituents in the fjord increase the  $C_1$ – $C_{14}$  distance ( $d_{1-14}$ ) and the helical pitch. The latter is expressed by a twist angle  $\theta$ , which is calculated as an average value of torsional angles of all phenanthrene subunits in [5]helicene. Alternative approaches to configurational stabilization include structural rigidification

through covalent locking of multiple [5]helicenes within a macrocycle. Cyclobis[5]helicenes, for instance, interconnect helicene units in a  $D_2$  symmetry structure, resulting in elevated racemization barriers (Figure 5.1).<sup>12,14</sup> Ultimate stabilization is achieved using topological locking, with fused [5]helicene dimers<sup>13</sup> and structures like infinitene or triply twisted Möbius carbon nanobelt,<sup>15,16</sup> which cannot racemize. These locking strategies have enabled the development of persistent, enantiopure helicene-based materials with tunable chiroptical properties.

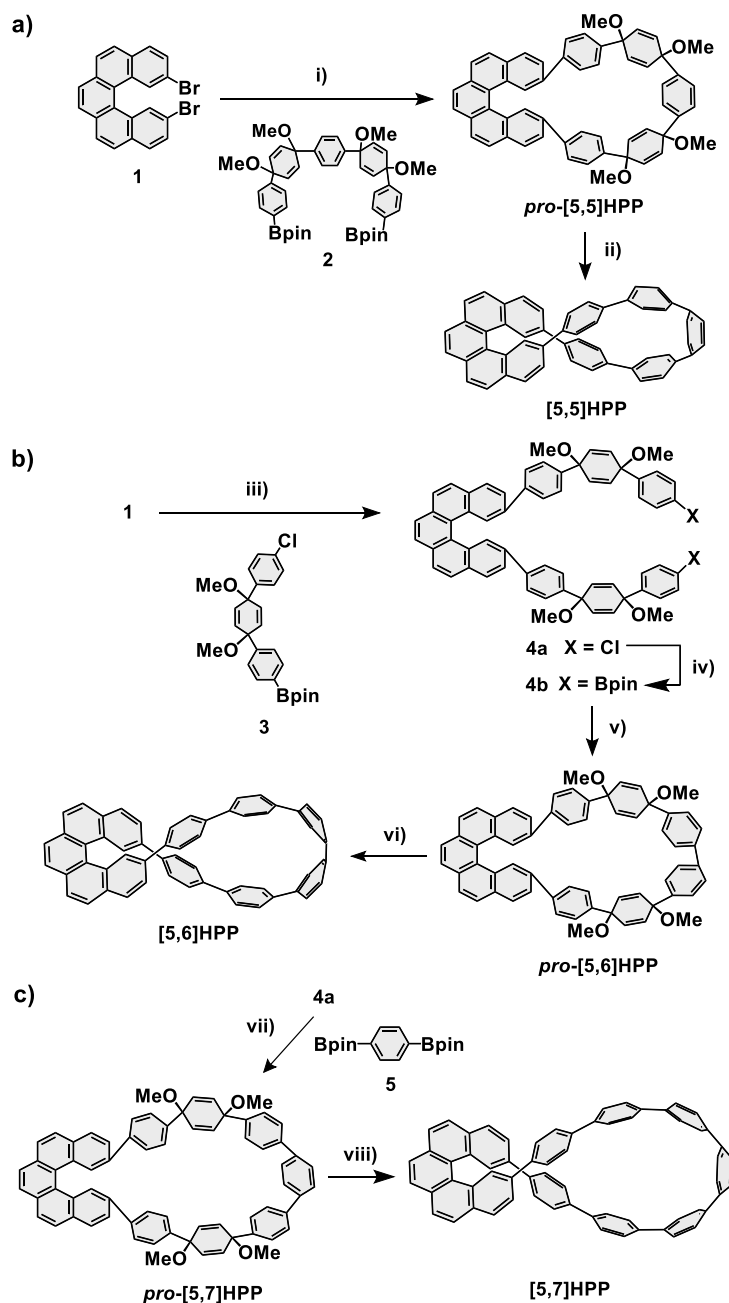
We previously reported the first [6]helicene-based chiral nanohoop, in which a single [6]helicene is formally embedded in highly strained [7]cycloparaphenylene ([7]CPP).<sup>17</sup> The resulting helicene *para*-phenylene ([6,7]HPP) displayed an unusual topological feature, namely, non-orientability of its  $\pi$ -electron system.<sup>18</sup> The compound exhibited remarkable configurational stability and strong, bright circularly polarized luminescence (CPL). Recently, we extended this design by embedding [5]helicene and benzothiadiazole (BTD) to [6]CPP creating<sup>19</sup> a bright CPL luminophore with  $\lambda_{em} > 650$  nm to test how excited state delocalization affects chiroptical properties of chiral nanohoops.<sup>20</sup> Despite lacking fjord substitution, the [5]helicene remained configurationally stable, showing no noticeable racemization over the course of extensive CPL measurements.

This led us to explore how strain in [5,*m*]HPPs (Figure 5.1), where *m* denotes the size of the embedding CPP, influences [5]helicene racemization. Strain in carbon nanohoops has been harnessed to enhance their reactivity, for instance, in click chemistry of alkyne-containing [*m*]CPPs,<sup>21</sup> their electrophilic bromination,<sup>22</sup> or in anthracene-dimer cycloreversion.<sup>23</sup> Strain also enabled efficient photo-uncaging of Fe<sup>2+</sup> from a ferrocene nanohoop.<sup>24</sup> However, a systematic experimental examination of strain in the racemization of a carbon nanohoop system is absent.<sup>25,26</sup>

## 5.2 Results and Discussion

We opted for the synthesis (Scheme 5.1) of a series of three helicene carbon nanohoops [5,*m*]HPPs (*m* = 5–7), where *m* controls the overall strain in the macrocycle. The synthesis of the smallest [5,5]HPP commences with Suzuki-Miyaura cross-coupling macrocyclization of 2,13-dibromo-[5]helicene<sup>27</sup> **1** with building block<sup>28</sup> **2** containing two pro-aromatic cyclohexadienes. We isolated the pro-aromatic macrocyclic *pro*-[5,5]HPP precursor in 23% yield after purification via recycling GPC (see the appendix). The *pro*-[5,5]HPP was subjected to reductive aromatization using H<sub>2</sub>SnCl<sub>4</sub> acid<sup>29</sup> affording [5,5]HPP in 80% isolated yield. The [5,6]HPP was synthesized through a Suzuki-Miyaura cross-coupling of **1** and building block **3**,<sup>30</sup> affording the intermediate **4a** in 80%

yield. Dichloride **4a** was subsequently subjected to Miyaura borylation to yield **4b**, followed by its oxidative homocoupling under conditions developed by Jasti and co-workers,<sup>31</sup> affording *pro*-[5,6]HPP in 52% yield over the two steps.



**Scheme 5.1.** i) 1 eq. **2**, 0.2 eq. Pd SPhos G3, 8 eq. K<sub>3</sub>PO<sub>4</sub>, dioxane:H<sub>2</sub>O = 10:1, 80 °C, 16 h, 24%. ii) 10 eq. H<sub>2</sub>SnCl<sub>4</sub>, THF, r.t., 1h, 80%. iii) 2 eq. **3**, 0.1 eq. Pd SPhos G3, 8 eq. K<sub>3</sub>PO<sub>4</sub>, dioxane:H<sub>2</sub>O = 10:1, r.t., 24 h, 80%. iv) 4 eq. (Bpin)<sub>2</sub>, 6.6 eq. KOAc, 0.05 eq. Pd<sub>2</sub>dba<sub>3</sub>, 0.2 eq. XPhos, dioxane, 80 °C, 16 h. v) 5 eq. B(OH)<sub>3</sub>, 20 eq. KF, 1 eq. Pd(PPh<sub>3</sub>)<sub>2</sub>Cl<sub>2</sub>, THF:H<sub>2</sub>O = 10:1, r.t., 16 h, 52% over two steps. vi) 2.2 eq. H<sub>2</sub>SnCl<sub>4</sub>, THF, r.t., 10 min, 97%. vii) 1.1 eq. **5**, 0.1 eq. Pd SPhos G3, 8 eq. K<sub>3</sub>PO<sub>4</sub>, dioxane:H<sub>2</sub>O = 10:1, 80 °C, 16 h. viii) 9 eq. H<sub>2</sub>SnCl<sub>4</sub>, THF, r.t., 30 min 25% over two steps.

Final reduction of *pro*-[5,6]HPP with  $\text{H}_2\text{SnCl}_4$  furnished [5,6]HPP in excellent 98% yield. The synthesis of [5,7]HPP commenced with a Suzuki-Miyaura cross-coupling of compounds **4a** and **5**, affording *pro*-[5,7]HPP, followed by its aromatization with  $\text{H}_2\text{SnCl}_4$  affording the desired nanohoop in 25% overall yield over two steps. All final compounds were characterized by  $^1\text{H}$  and  $^{13}\text{C}$  NMR spectroscopy and high-resolution mass spectrometry. We note that during writing this manuscript, Jiang reported a different synthesis of [5,7]HPP,<sup>32</sup> but not its stereodynamic behavior.

**Photophysical properties of synthesized compounds:** The absorption and emission spectra of the [5,*m*]HPP series were measured to elucidate the influence of ring size on the optical properties (Figure 5.2). As expected, the calculated strain energy in individual compounds increases as the size of the macrocycle decreases ( $E_{\text{strain}}$ , Table 5.1). All three HPPs exhibit a prominent absorption maximum at  $\lambda_{\text{abs}} = 340$  nm characteristic of CPP systems.<sup>33</sup> A distinct shoulder at  $>400$  nm is observed in all spectra, corresponding to the HOMO–LUMO transition that reflects the curvature of the nanohoops.

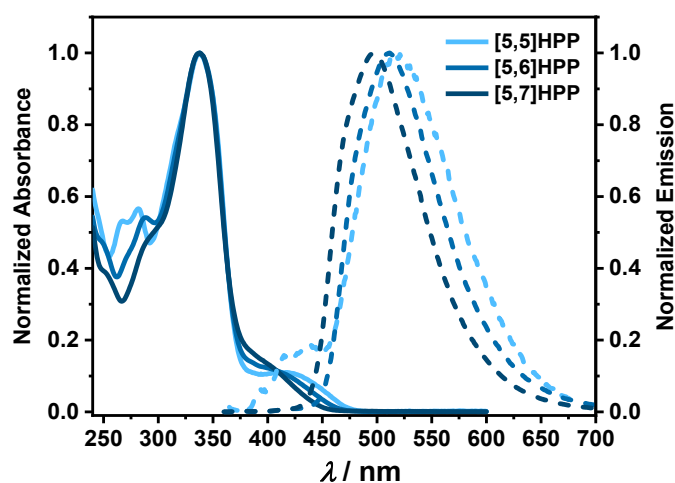


**Figure 5.2.** Absorption (solid lines) and emission (dotted lines) spectra of [5,*m*]HPPs ( $m = 5-7$ ) in dichloromethane ( $c \sim 10^{-6}$  M).

The smallest, most strained [5,5]HPP displays the most red-shifted transition, resulting in a separate absorption band at 419 nm. The recorded emission maxima  $\lambda_{\text{em}}$  indicate a slight red-shift as the nanohoop size decreases, which is consistent with narrowing the HOMO–LUMO energy gap known for CPPs (Table 5.1). Notably, the fluorescence quantum yield ( $\phi_{\text{f}}$ ) increases with increasing ring size, suggesting that non-radiative decay channels are suppressed in larger HPPs more efficiently.

**Chiral HPLC and kinetics experiments:** We separated the enantiomers of all three nanohoops using recycling HPLC with a chiral stationary phase to obtain samples of individual enantiomers with >99% enantiomeric excess (*ee*). The configurations of the isolated enantiomers were assigned using electronic circular dichroism spectroscopy, quantum chemical calculations, and HPLC data (Figures A5.8-5.12, A5.21). We did not observe any racemization in the samples of **[5,6]HPP** and **[5,7]HPP** over several days at room temperature. However, we noticed partial conversion of enantiomers of **[5,5]HPP**. This indicated that the strain in the compounds affects their configurational stability. The racemization of [5,*m*]HPPs was thus investigated by monitoring the evolution of the sample *ee* as a function of time at elevated temperatures (65–100°C). The process was stopped by rapid cooling of the sample solution at selected time intervals, and the concentration of enantiomers was quantified by analytical HPLC (details in appendix). As expected, the *ee* gradually decreased with time following the first-order rate law. The linear plots of  $\ln(ee_t/ee_{t=0})$  vs. *t* permitted extracting the corresponding enantiomerization rate constants ( $k_{\text{en}}$ , Figures A5.13-A5.18). The activation free energies ( $\Delta G_{\text{T}}^\ddagger$ ; T is temperature; Table 5.1) were then obtained from  $k_{\text{en}}$ . In addition, we evaluated the  $\Delta G_{\text{T}}^\ddagger$  at different temperatures (Figure 5.3, Figures A5.19-A5.20) to estimate if the process is driven by the activation enthalpy ( $\Delta H^\ddagger$ ) and entropy ( $\Delta S^\ddagger$ ). Prolonged heating, however, decomposes the nanohoops, especially **[5,5]HPP**. Additionally, the presence of oxygen facilitates decomposition even at room temperature. Therefore, the experiments were performed with deoxygenated samples under argon. Thereby we have observed much faster racemization than decomposition.

**Table 5.1.** Photophysical properties and Racemization kinetics parameters:

Molecule	$\lambda_{\text{em}}$ / nm	$\phi_{\text{fl}}$	$\tau_{\text{fl}}$ / ns	$E_{\text{strain}}^a$ kcal mol <sup>-1</sup>	$\Delta G_{\text{T}}^\ddagger$ <sup>363</sup> kcal mol <sup>-1</sup>	$\Delta H^\ddagger$ <sup>b</sup> kcal mol <sup>-1</sup>	$\Delta S^\ddagger$ <sup>b</sup> cal mol <sup>-1</sup> K <sup>-1</sup>	$\Delta H_{\text{en}}^\ddagger$ <sup>c</sup> kcal mol <sup>-1</sup>
<b>[5]helicene</b>	424 <sup>d</sup>	0.04 <sup>d</sup>	26 <sup>d</sup>	0.0	24.4 <sup>e</sup>	22.9	-4.1	24.7
<b>[5,5]HPP</b>	518	<0.01	— <sup>f</sup>	61.9	25.5 <sup>g</sup> ± 0.070	26.8 ± 2.62	3.7 ± 7.92	26.2
<b>[5,6]HPP</b>	512	0.29	2.5	55.5	27.7 <sup>h</sup> ± 0.060	36.3 ± 1.24	23.4 ± 3.48	29.4
<b>[5,7]HPP</b>	498	0.46	2.6	50.0	28.5 <sup>h</sup> ± 0.030	32.5 ± 0.82	10.8 ± 2.25	30.4

<sup>a</sup>Calculated using homodesmotic reaction approach (B3LYP-D3/cc-pVTZ; see the appendix). <sup>b</sup>From Eyring analysis. <sup>c</sup>Calculated (0K, MN15/cc-pVTZ, see the appendix for other functionals). <sup>d</sup>Reported previously.<sup>34,35</sup> <sup>e</sup>Calculated from  $\Delta G_{\text{T}}^\ddagger = \Delta H^\ddagger - T\Delta S^\ddagger$ .<sup>11</sup> <sup>f</sup>Not available. <sup>g</sup>Experimental value at 338K. <sup>h</sup>Experimental value.

The  $\Delta G_{\text{T}}^\ddagger$  for all nanohoops is higher than that of parent [5]helicene ( $\Delta G_{298}^\ddagger = 24.1$  kcal mol<sup>-1</sup>) and demonstrates that helicene incorporation into a nanohoop increases its configurational stability. Clearly, the free energy barriers do not reach values of fjord-substituted [5]helicenes, but they show a trend that correlates with the strain in the nanohoop. While the smallest, most strained **[5,5]HPP** attains a modest increase in the configurational stability with  $\Delta G_{298}^\ddagger = 25.7$  kcal mol<sup>-1</sup>, the larger

HPPs possess  $\Delta G_{298}^\ddagger > 28.5 \text{ kcal mol}^{-1}$ , sufficient to maintain their enantiomeric purity for months at room temperature. The higher  $\Delta G_{\text{T}}^\ddagger$  in the larger HPPs with fjord-free [5]helicene appears counterintuitive. A large nanohoop with smaller strain is expected to behave closer to [5]helicene than a small, strained nanohoop. However, both the helicene and the curved *para*-phenylenes<sup>36</sup> must change their geometry to reach the transition state structure. To gain additional insight into the enantiomerization pathway and the effect of the individual units in HPPs, we performed DFT calculations for all three [5,*m*]HPPs, 2,13-diphenyl-[5]helicene, and parent [5]helicene.

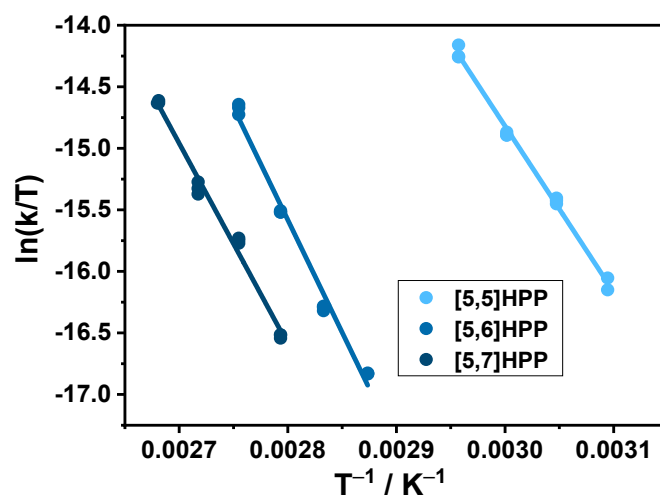
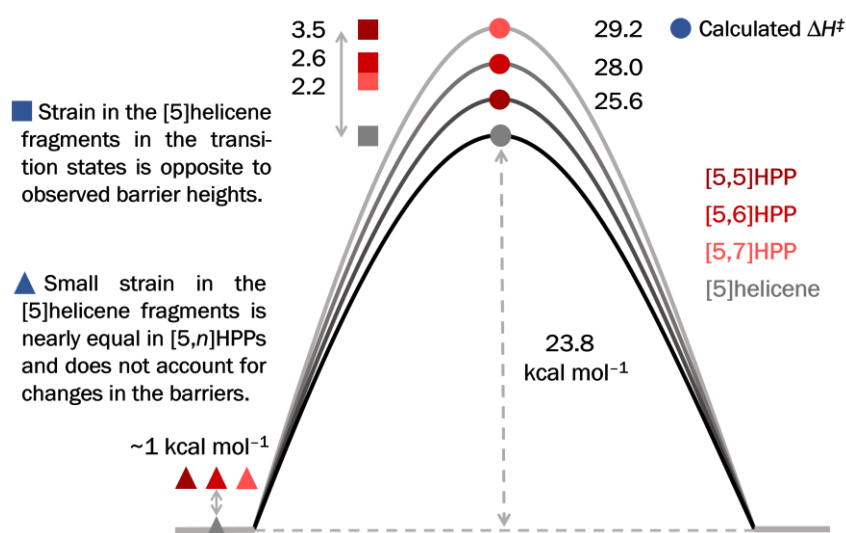


Figure 5.3. Eyring plots for [5,*m*]HPPs.

All [5,*m*]HPPs adopt a variety of conformations. Therefore, we performed a thorough conformational search, which confirmed that the lowest energy conformers of all HPPs display non-orientable  $\pi$ -electron systems (Figure A5.22), a feature observed previously in the crystal structures of [6,7]HPP<sup>17</sup> and [5,7]HPP.<sup>32</sup> We tried to locate the transition states for each individual conformer. However, we found that the optimizations tend to relax to geometries that are close to  $C_s$  symmetry (Figure A5.24), the symmetry of the transition state structure of [5]helicene.<sup>10</sup> These possess the lowest energies and are thus considered further. The calculated  $\Delta H^\ddagger$  (Table 5.1, Table A5.10) shows the same trend as observed for experimental  $\Delta G_{\text{T}}^\ddagger$ , *i.e.*, the larger the HPP, the higher the barrier. The calculations thus indicate that the enantiomerization process is driven by enthalpy, the same conclusion obtained from our experiments, and the activation entropy is small (Table A5.12). The low  $\Delta S^\ddagger$  agrees well with the experimental data for [5]helicene and its derivatives and validates our theoretical method.<sup>8,11</sup> Although the experimental  $\Delta S^\ddagger$  for [5,5]HPP and [5,7]HPP is relatively small, in good agreement with the calculations, the experimental values of  $\Delta H^\ddagger$  and  $\Delta S^\ddagger$  determined for [5,6]HPP are too high. It appears that our

$\Delta H^\ddagger$  and  $\Delta S^\ddagger$  data may contain a systematic experimental error, especially those for **[5,6]HPP**, which results in the enthalpy–entropy compensation. We note that estimating accurate enantiomerization  $\Delta S^\ddagger$  using a limited range of temperatures can be challenging.<sup>37,38</sup> Extending the range of temperature in our case is, however, not feasible. At lower temperatures, the rate of the process is too low to be observable within reasonable amount of time. At higher temperatures, we observe that a decomposition process starts competing with racemization despite deoxygenating the solutions. Moreover, the additional source of error in our experiments can be the uncertainty in the experimental temperature, which is  $\pm 0.5$  K. As a result, our Eyring analysis should be treated as semiquantitative at most, yet confirming that enantiomerization of **[5,*n*]HPPs** is driven by  $\Delta H^\ddagger$ .

### Dissecting strain contribution in the racemization



**Figure 5.4.** DFT analysis of the strain–barrier relationship (B3LYP-D3/cc-pVTZ energies in kcal mol<sup>-1</sup>; see the appendix).

Importantly, we do not observe any correlation of the height of the barriers with structural parameters of [5]helicene (Table A5.11), such as  $d_{1-14}$  or  $\theta$ , as in the non-covalently stabilized fjord-substituted [5]helicene derivatives.<sup>8</sup> The barrier is thus likely determined by the strain in the transition states, which agrees with the calculated  $\Delta H^\ddagger$ . Therefore, we dissected the effect of strain in the structures of HPPs’ “ground” and transition states. Unlike in CPPs, the strain is not distributed equally in HPPs. Visualization of the strain energy distribution obtained by StrainViz (Figure A5.23) shows that the distant phenylenes are the most strained in HPPs, in agreement with our previous theoretical and experimental work on **[6,7]HPP**.<sup>17</sup> Calculations show that individual [5]helicenes are strained by  $\sim 1$  kcal mol<sup>-1</sup> in all HPPs (Table A5.9), a value calculated also for 2,13-diphenyl-[5]helicene. Such destabilization does not reproduce the observed activation parameters.

Comparison of the geometries and energies of [5]helicene fragments (see the appendix) in the transition states portrays a clearer picture (Figure 5.4). It can be summarized as follows: (i) Their strain is larger in the transition states; (ii) the configurational stabilization of **[5,5]HPP** can be explained nearly exclusively by the strain imposed on its [5]helicene in the transition state (Table A5.9); (iii) the additional strain imposed by curved *para*-phenylenes must hinder the enantiomerization in the larger **[5,6]HPP** and **[5,7]HPP**. The CPP formally embedding the [5]helicene thus provides additional configurational stabilization as the curved segment tends to adopt the  $C_s$  symmetry of the [5]helicene transition state, which imparts additional strain on the most distant *para*-phenylenes. Since the larger macrocycles are less strained in their energy minimum, the increase of the strain is somewhat larger for those with longer *para*-phenylene segments. This suggests that the barrier for **[5,8]HPP** should be even higher than that for **[5,7]HPP**. We thus calculated the corresponding  $\Delta H^\ddagger$  to verify this prediction.

Indeed, the calculated  $\Delta H^\ddagger$  (Table A5.10) increased by additional  $>1$  kcal mol<sup>-1</sup>, which underpins our analysis. We note that the trend must saturate by enlarging the size of the nanohoops beyond certain point because the strain energy in a large macrocycle will change only subtly by adding an extra phenylene. We speculate that the  $\Delta G^\ddagger$  may start decreasing afterwards as we expect that enantiomerization of [5]helicene in an infinitely large macrocycle resembles that of 2,13-diphenyl-[5]helicene.

### 5.3 Conclusion

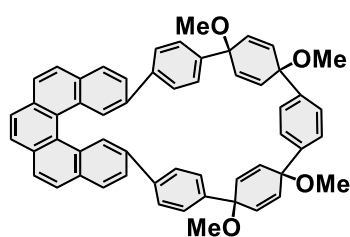
In conclusion, we synthesized a series of chiral carbon nanohoops that embed [5]helicene, separated their enantiomers, and investigated the effect of the nanohoop strain on their stereodynamic behavior. Thereby, we revealed a structure–property relationship that establishes design principles to control stereodynamics of [5]helicenes with a free fjord region, a concept that is straightforward to extend to other (hetero)helicene derivatives.

## 5.4 Appendix

**General remarks:** Additional material that can be found in the Supporting Information of the published paper (<https://doi.org/10.1021/acs.joc.5c02280>): General experimental details, synthetic procedures and compound characterization data for 4a, 4b, *pro*-[5,6]HPP, [5,6]HPP, [5,6]HPP, stability of [5,*n*]HPPs, first order decay data (tables of ee vs time) for [5,*n*]HPPs, rate constants and racemization kinetics data for [5,*n*]HPPs, UV-vis and CD dilution series, calculated CD spectra and excited-state lifetime measurements for [5,6] and [5,7]HPP, cartesian coordinates.

9,12-Dibromo-[5]helicene **1** was prepared according to a modified procedure by Moorthy et al.<sup>27</sup> **2** and **3** were prepared according to a procedure by Jasti et al.<sup>28,39</sup> **5** is commercially available.

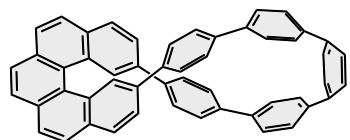
### Synthesis of *pro*-[5,5]HPP:



**1** (70 mg; 0.16 mmol; 1.00 equiv) and **2** (130 mg; 0.18 mmol; 1.10 equiv) were weighed in a Schlenk flask and dissolved in dioxane (120 mL) and H<sub>2</sub>O (12 mL). The resulting solution was deoxygenated by bubbling with Ar for 1 h. K<sub>3</sub>PO<sub>4</sub> (270 mg; 1.3 mmol; 8.00 equiv) and SPhos Pd G3 (25 mg; 32 μmol; 0.2 equiv) were added, and the degassing continued for 30 min. The Schlenk flask was sealed and

placed into an oil bath preheated to 80 °C. The reaction was stirred for 18 h at 80 °C. The reaction mixture was filtered through Celite, the flask and Celite were rinsed with dichloromethane and the volatiles were evaporated, and the crude product was purified using column chromatography (40% EtOAc in petroleum ether) followed by recycling GPC using chloroform. The product was isolated as a white solid (30 mg, 24%). **<sup>1</sup>H NMR** (300 MHz, CDCl<sub>3</sub>, 298 K, δ/ppm): 8.87 (d, *J* = 1.6 Hz, 2H), 8.03 (d, *J* = 8.3, 2H), 7.96 (d, *J* = 8.5 Hz, 2H), 7.89 (t, *J* = 4.3 Hz, 4H), 7.65 (dd, *J* = 8.3, 1.7 Hz, 2H), 7.34 (s, 8H), 7.12 (s, 4H), 6.31 (dd, *J* = 10.3, 2.4 Hz, 2H), 6.15–6.07 (m, 4H), 5.94 (dd, *J* = 10.1, 2.4 Hz, 2H), 3.44 (s, 6H), 3.33 (s, 6H). **<sup>13</sup>C NMR** (75 MHz, CDCl<sub>3</sub>, 298 K, δ/ppm): 142.0, 141.9, 141.4, 137.8, 134.5, 134.5, 133.3, 132.7, 132.6, 132.2, 131.8, 131.2, 128.7, 128.4, 127.9, 127.5, 127.3, 127.2, 126.8, 126.8, 126.6, 126.0, 126.0, 125.6, 75.5, 74.5, 52.2, 52.0. **HRMS (FD, +):** *m/z* calcd. for C<sub>56</sub>H<sub>44</sub>O<sub>4</sub>: 780.3240, found: 780.3232.

### Synthesis of [5,5]HPP:



Macrocycle *pro*-[5,5]HPP (10 mg; 13 μmol; 1.00 equiv) was dissolved in THF (3 mL) and degassed for 30 min and H<sub>2</sub>SnCl<sub>4</sub> (127 mM in THF; 1.0 mL; 0.13 mmol; 10 equiv) was added. The reaction mixture was stirred for 1 h at room temperature and quenched with

10% aqueous NaOH (1 mL). The resulting mixture was diluted with H<sub>2</sub>O (10 mL) and extracted with DCM (3 times 10 mL). The combined organic phases were washed with brine (10 mL) and dried with Na<sub>2</sub>SO<sub>4</sub>, and the volatiles were evaporated. The crude product was purified on recycling GPC using chloroform. The product was isolated as a yellow solid (7 mg; 80%). A reduced stability of this compound was observed in solution (slight decomposition overnight in CDCl<sub>3</sub>/CD<sub>2</sub>Cl<sub>2</sub>). **<sup>1</sup>H NMR** (300 MHz, CD<sub>2</sub>Cl<sub>2</sub>, 298 K, δ/ppm): δ 8.86 (d, *J* = 1.7 Hz, 2H), 8.07 (d, *J* = 8.4 Hz, 2H), 7.98 (d, *J* = 8.5 Hz, 2H), 7.92–7.85 (m, 4H), 7.63 (td, *J* = 9.1, 2.0 Hz, 6H), 7.41 (dd, *J* = 9.3, 2.2 Hz, 4H), 7.33–7.20 (m, 12H). **<sup>13</sup>C NMR** (101 MHz, CD<sub>2</sub>Cl<sub>2</sub>, 298 K, δ/ppm): 139.9, 139.2,

139.0, 137.4, 137.0, 136.9, 133.2, 132.6, 132.2, 129.9, 129.5, 128.2, 128.1, 127.9, 127.8, 127.7, 127.5, 126.8, 126.6, 124.2. **HRMS (FD, +):**  $m/z$  calcd. for  $C_{52}H_{32}$ : 656.2504, found: 656.2505.

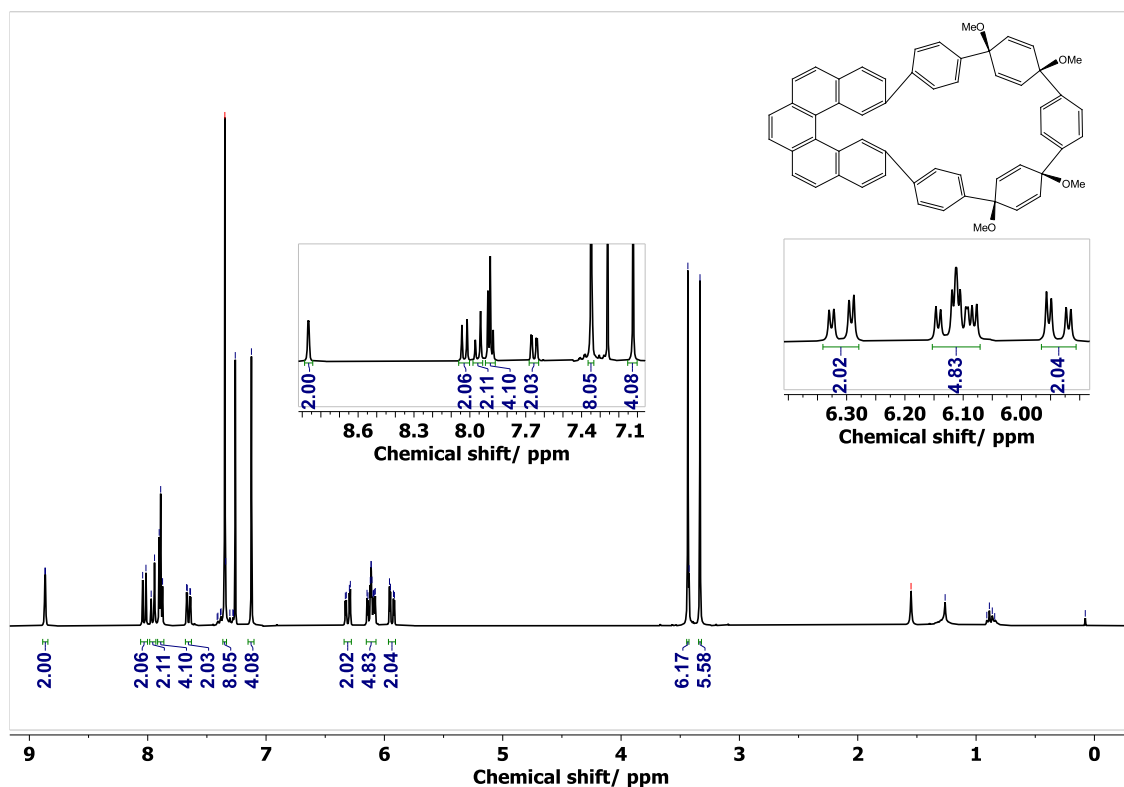


Figure A5.1.  $^1\text{H-NMR}$  (300 MHz,  $\text{CDCl}_3$ , 298 K) spectrum of *pro*-[5,5]HPP.

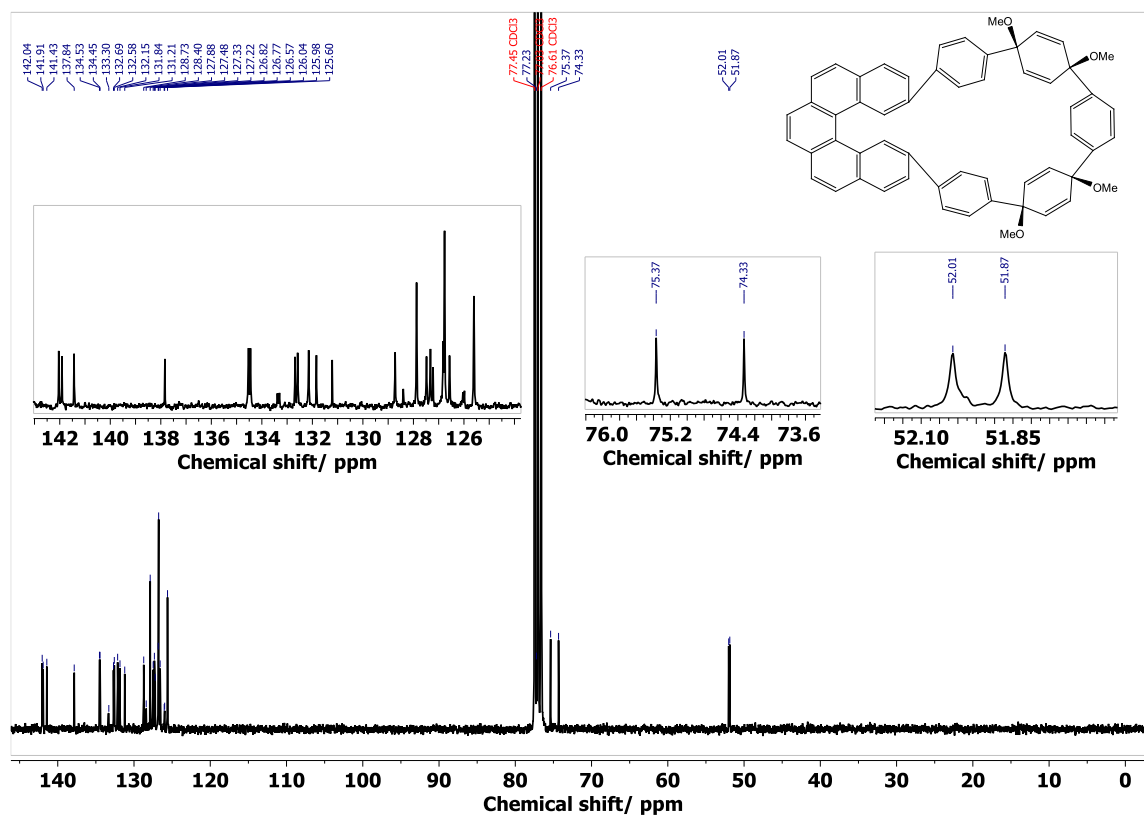


Figure A5.2.  $^{13}\text{C}\{^1\text{H}\}$ -NMR (126 MHz,  $\text{CDCl}_3$ , 298 K) spectrum of *pro*-[5,5]HPP.

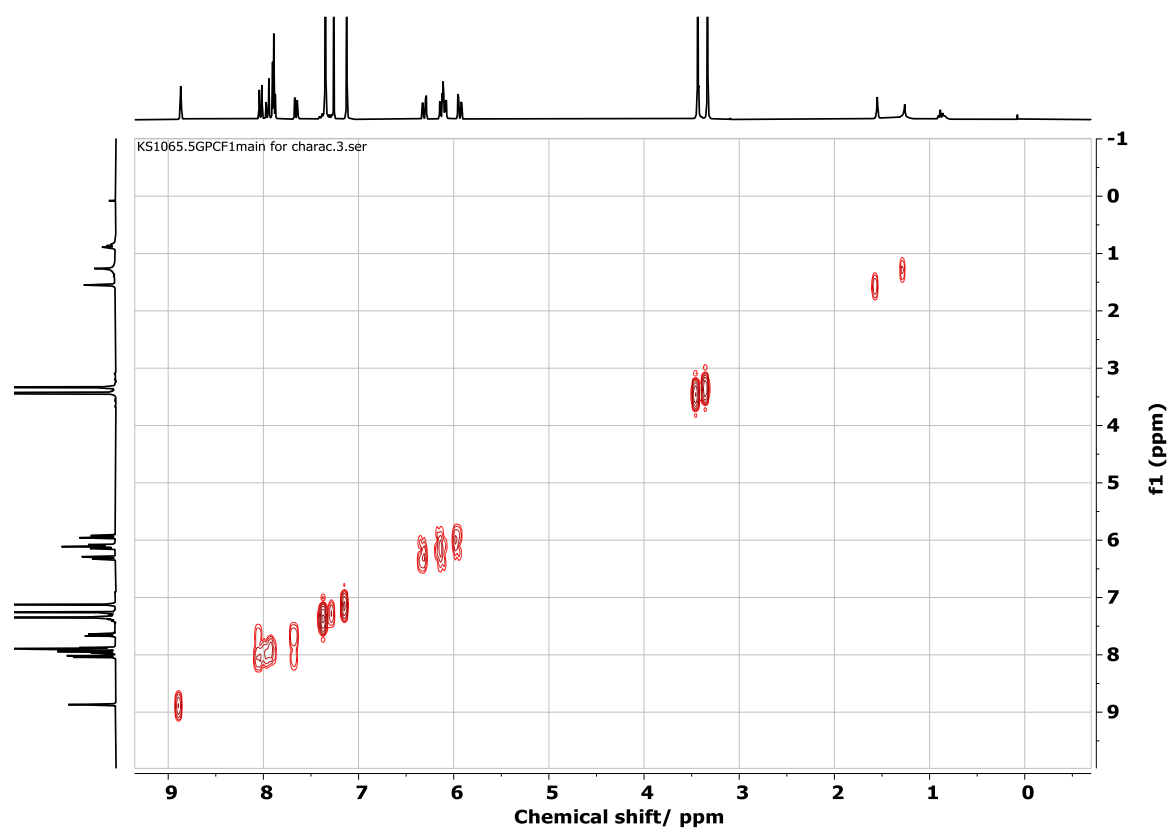


Figure A5.3.  $^1\text{H}$ - $^1\text{H}$  COSY ( $\text{CDCl}_3$ , 298 K) spectrum of *pro*-[5,5]HPP.

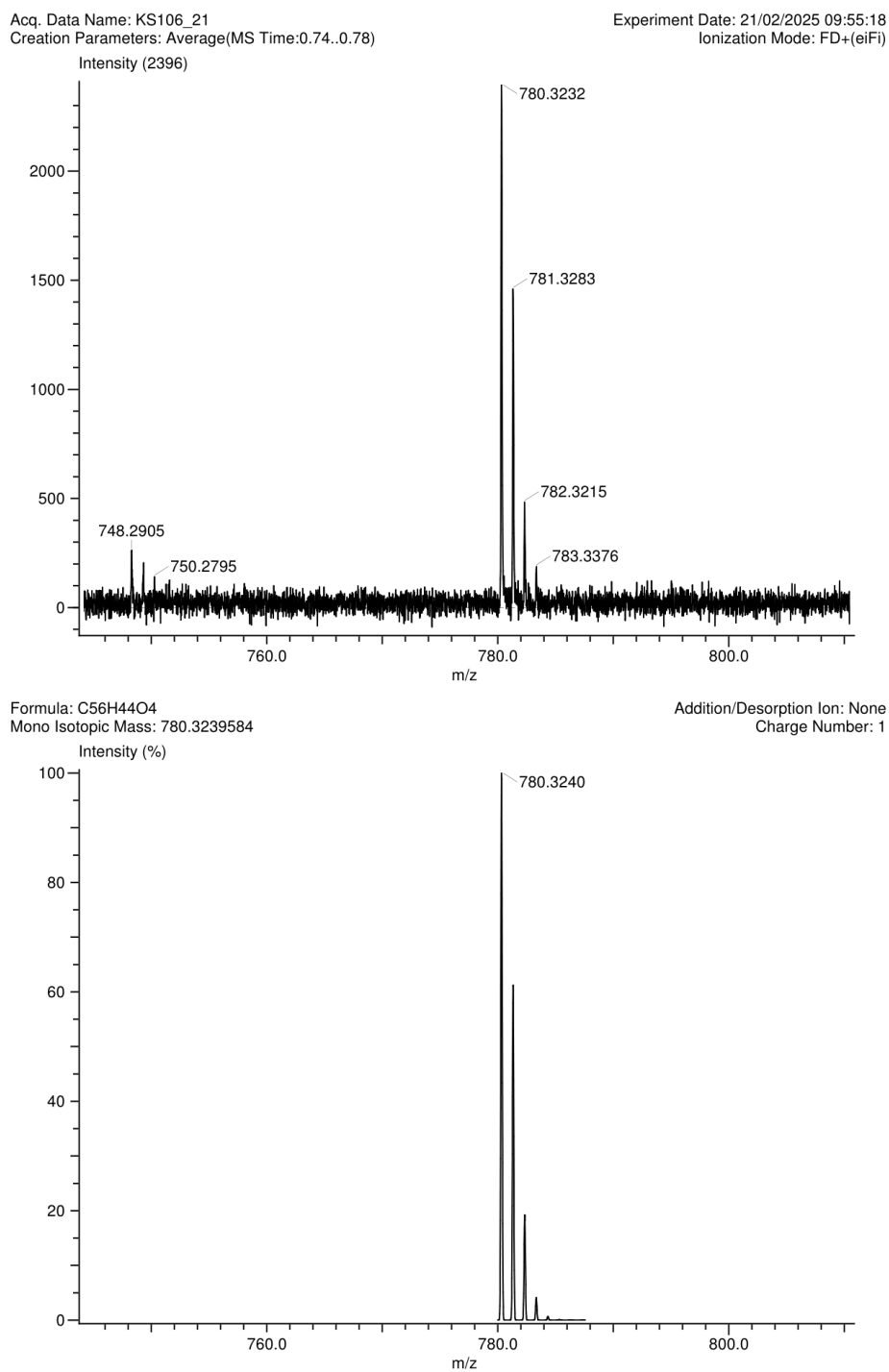


Figure A5.4. HR-MS (FD+) spectrum of *pro*-[5,5]HPP.

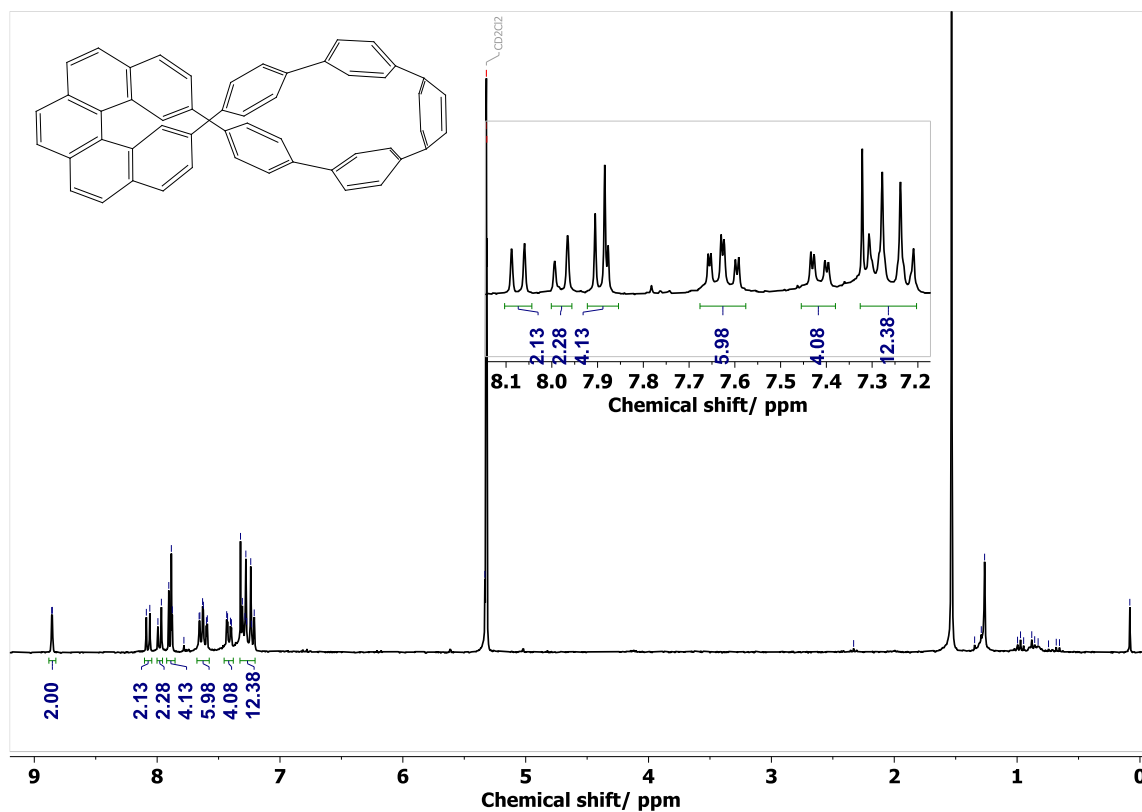


Figure A5.5.  $^1\text{H-NMR}$  (300 MHz,  $\text{CD}_2\text{Cl}_2$ , 298 K) spectrum of [5,5]HPP.

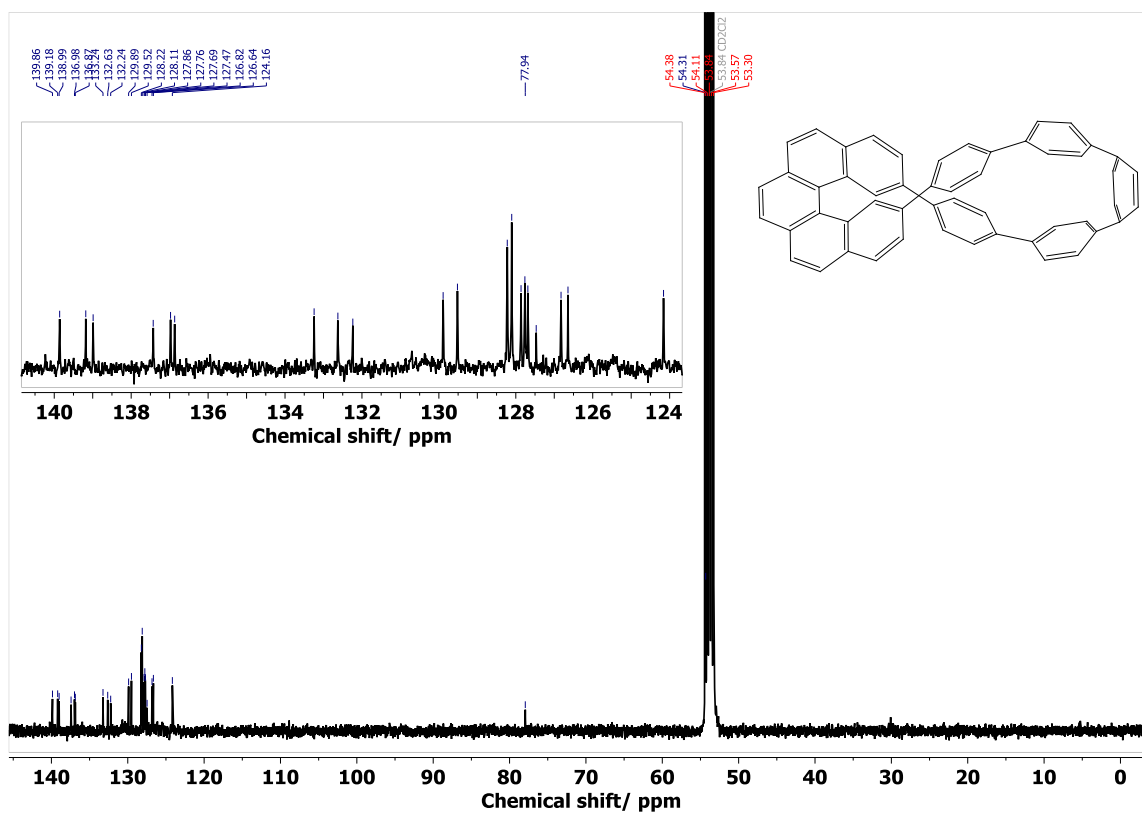


Figure A5.6.  $^{13}\text{C}\{^1\text{H}\}$ -NMR (126 MHz,  $\text{CD}_2\text{Cl}_2$ , 298 K) spectrum of [5,5]HPP.

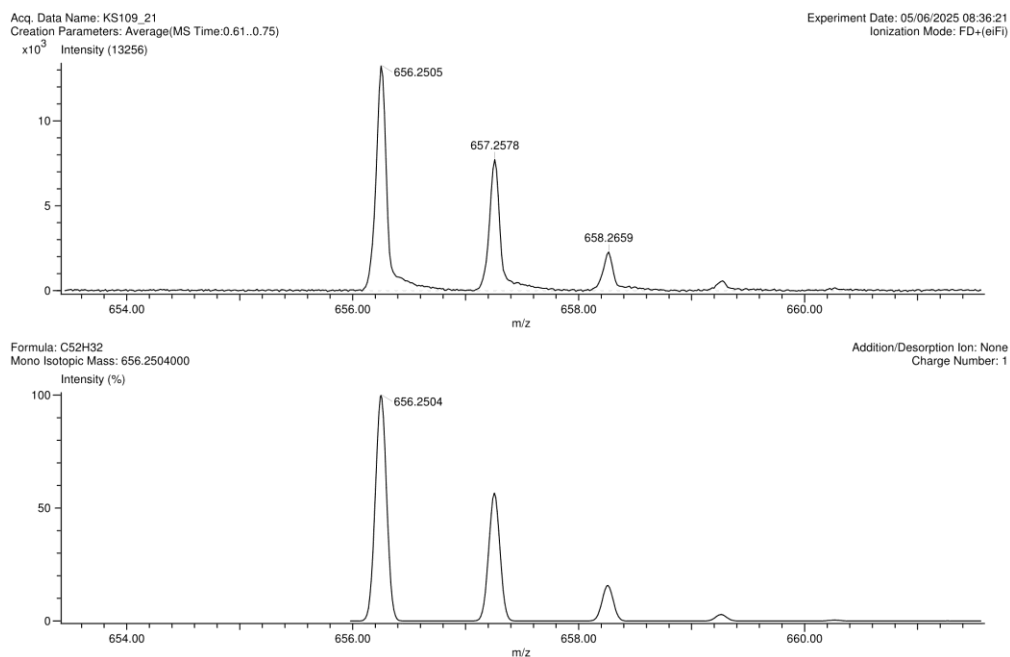


Figure A5.7. HR-MS (FD+) spectrum of [5,5]HPP.

**Preparative HPLC:** 5 mg of a racemic [5,5]HPP was dissolved in 5 mL of DCM/heptane = 1/1 mixture, filtered with a syringe filter and injected into the HPLC equipped with Chiralpak IG (20×250) mm column by Daicel Chemical Industries Ltd. DCM/heptane = 1/1 was used as eluent at 10 mL min<sup>-1</sup> flow rate.

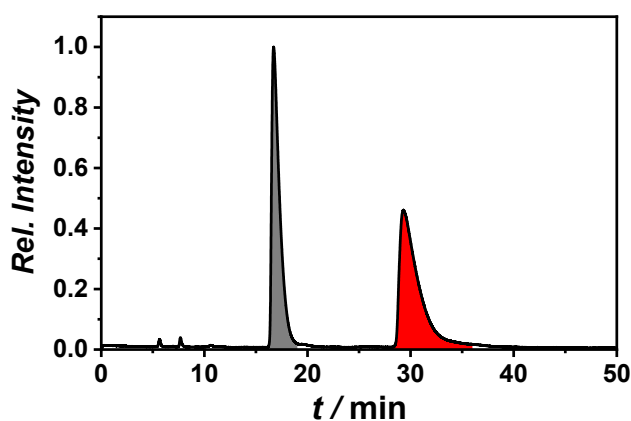
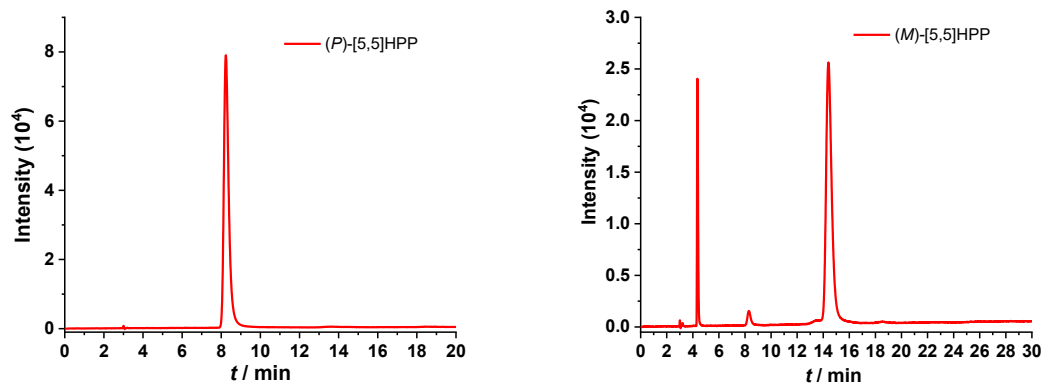
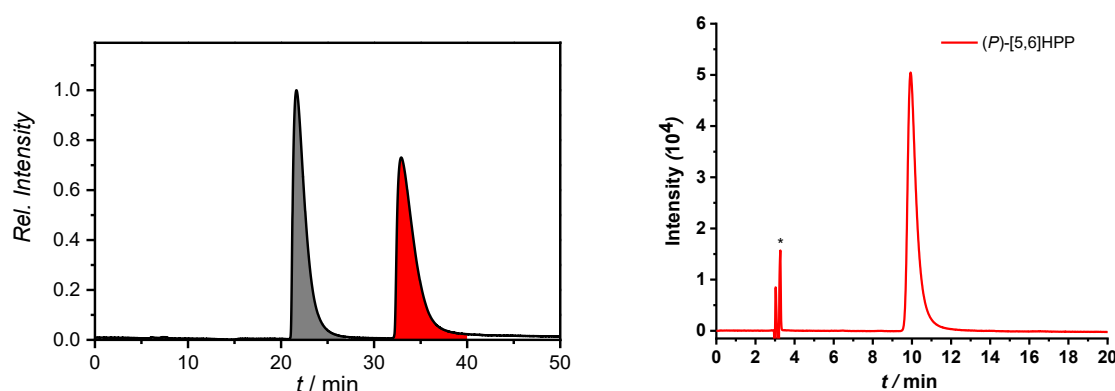


Figure A5.8. Preparative HPLC chromatogram of [5,5]HPP with (*P*)-enantiomers (grey) eluting first followed by (*M*)-enantiomers (red).



**Figure A5.9.** HPLC chromatogram of (*P*)-[5,5]HPP (left) and (*M*)-[5,5]HPP (right) in 1:1 DCM/heptane mixture (flow rate 1 ml/min) used for racemization experiments. Due to presence of small amounts of (*P*) enantiomer (right), this enantiomer was not used for experiments.

10 mg of a racemic [5,6]HPP was dissolved in 5 mL of DCM and diluted with 5 mL of heptane. The resulting solution was filtered with a syringe filter and injected into the HPLC equipped with Chiralpak IG, 5  $\mu\text{m}$ , 30 $\times$ 250 mm column by Daicel Chemical Industries Ltd. DCM/heptane = 1/1 was used as eluent at 20 mL min<sup>-1</sup> flow rate. The chromatogram shown in Figure A5.10 was recorded one month after the initial chiral HPLC resolution, and the enantiomeric separation remained stable over this period.



**Figure A5.10.** Preparative HPLC chromatogram of [5,6]HPP (left) with (*P*)-enantiomers (grey) eluting first followed by (*M*)-enantiomers (red). HPLC chromatogram of (*P*)-[5,6]HPP (right) in 1:1 DCM/heptane mixture (flow rate 1 ml/min) used for racemization experiments. \* = injection peak. Enantiopure (*M*)-[5,6]HPP was not obtained, therefore (*P*)-[5,6]HPP was used for the racemization kinetics.

4.7 mg of a racemic [5,7]HPP was dissolved in 5 mL of DCM/heptane = 1/1 mixture, filtered with a syringe filter and injected into the HPLC equipped with Chiralpak IG, 5  $\mu\text{m}$ , 30 $\times$ 250 mm column by Daicel Chemical Industries Ltd. DCM/heptane = 1/1 was used as eluent at 20 mL/min flow rate. The chromatograms shown in Figure A5.12 were recorded one month after the initial chiral HPLC resolution, and the enantiomeric separation remained stable over this period.

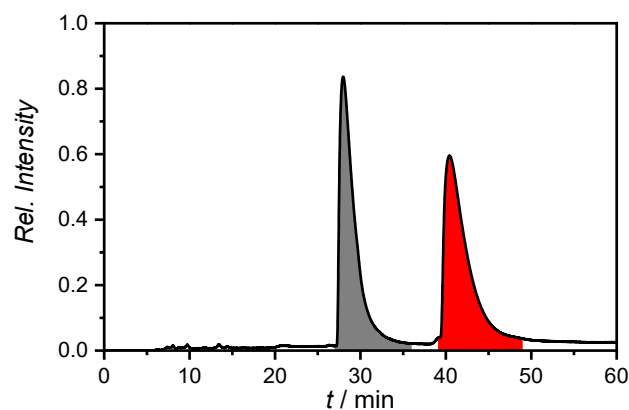


**Figure A5.11.** Preparative HPLC chromatogram of [5,7]HPP with (*P*)-enantiomers (grey) eluting first followed by (*M*)-enantiomers (red).

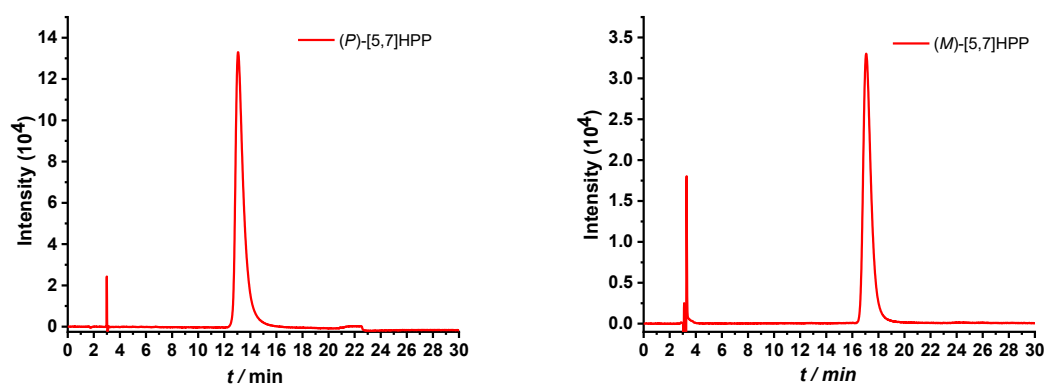


**Figure A5.12.** HPLC chromatogram of (*P*)-[5,7]HPP (left) and (*M*)-[5,7]HPP (right) in 1:1 DCM/heptane mixture (flow rate 1 ml/min). (*M*)-[5,7]HPP was used for racemization experiments.

**Racemization Kinetics:** Extensive racemization kinetics experiments were performed for the [5,*n*]HPP series. At each studied temperature, three independent sample stock solutions were prepared in three vials by dissolving 1 mg of enantiopure nano hoop each in 1 ml toluene and the samples were degassed for 30 min. All three sample vials were then placed on a heated plate at the temperature of interest (the temperature deviation for the experimental determination of racemization was no more than  $\pm 0.5$  °C) and samples were collected over time from each vial at each time point, cooled down to room temperature and injected into the analytical HPLC equipped with a chiralpak IG column ( $4.6 \times 250$ ) using DCM-*n*-heptane (1:1) as the eluent and  $1 \text{ ml min}^{-1}$  flow rate. Kinetics experiments were performed at temperatures ranges of 50–65, 75–90, and 85–100 °C for [5,5]HPP, [5,6]HPP and [5,7]HPP, respectively. Enantiomeric excess (ee) was calculated using the ratios of areas under the peaks in the HPLC chromatograms. The enantiomeric excess was plotted against time (*t*) to calculate the rate constants of racemization ( $k_{\text{rac}}$ ) which gave access to the rate constants of enantiomerization ( $k_{\text{en}}$ ).<sup>37</sup> Further, the activation barriers of racemization ( $\Delta G^\ddagger$ ) were calculated for all the nano hoops at different temperatures. Using the Eyring equation, other thermodynamic parameters such as the activation enthalpy ( $\Delta H^\ddagger$ ) and

entropy ( $\Delta S^\ddagger$ ) were also extracted. The rate constants  $k_{rac}$ ,  $k_{en}$ , half-life,  $\Delta G^\ddagger$ ,  $\Delta H^\ddagger$  and  $\Delta S^\ddagger$  were determined using the following equations:

$$ee(t) = ee_0 \cdot e^{-k_{rac}t} \quad (1)$$

$$k_{en} = \frac{k_{rac}}{2} \quad (2)$$

$$\tau = \frac{\ln 2}{k_{en}} \quad (3)$$

$$\ln \frac{k_{en}}{T} = -\frac{\Delta H^\ddagger}{R} \frac{1}{T} + \ln \frac{k_B}{h} + \frac{\Delta S^\ddagger}{R} \quad (4)$$

$$\Delta G^\ddagger = \Delta H^\ddagger - T\Delta S^\ddagger \quad (5)$$

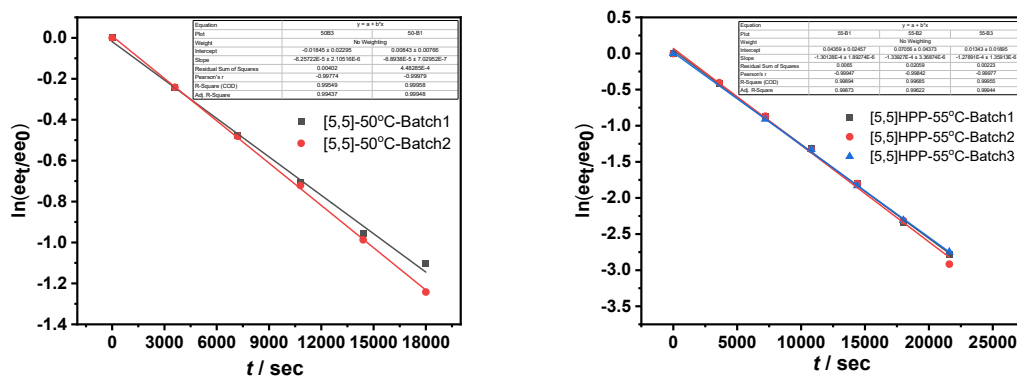


Figure A5.13. First order decay plots from three independent measurements for [5,5]HPP at 50°C (left) and 55°C (right).

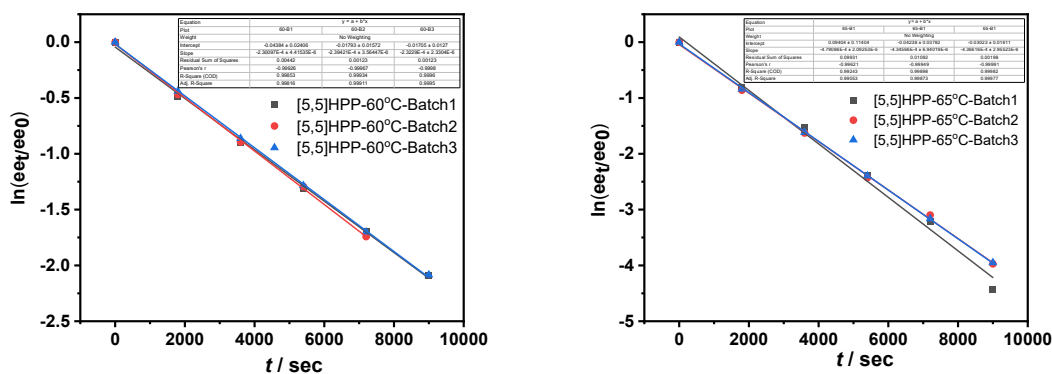


Figure A5.14. First order decay plots from three independent measurements for [5,5]HPP at 60°C (left) and 65°C (right).

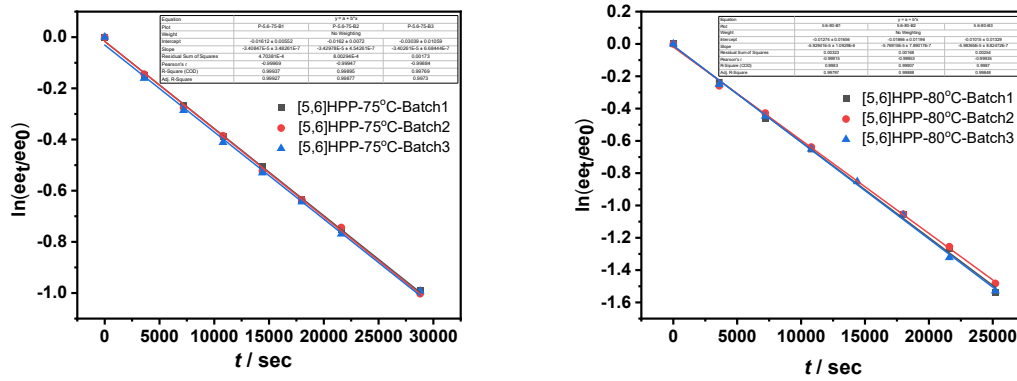


Figure A5.15. First order decay plot from three independent measurements for [5,6]HPP at 75°C (left) and 80°C (right).

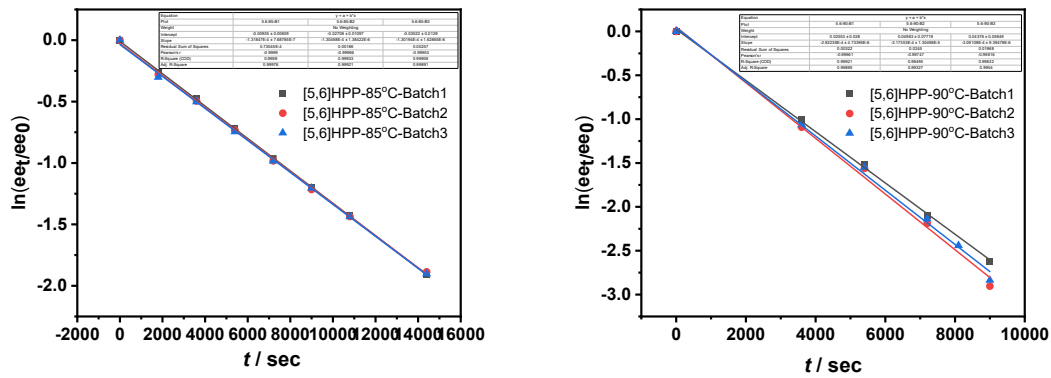


Figure A5.16. First order decay plots from three independent measurements for [5,6]HPP at 85°C (left) and 90°C (right).

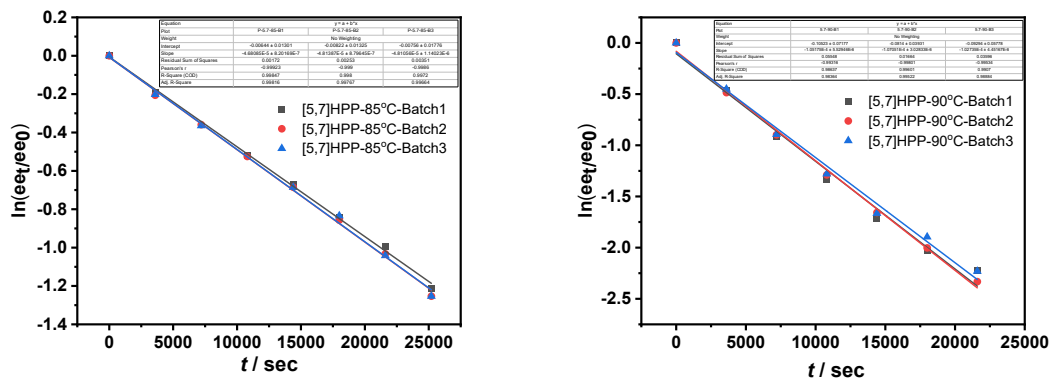


Figure A5.17. First order decay plots from three independent measurements for [5,7]HPP at 85°C (left) and 90°C (right).

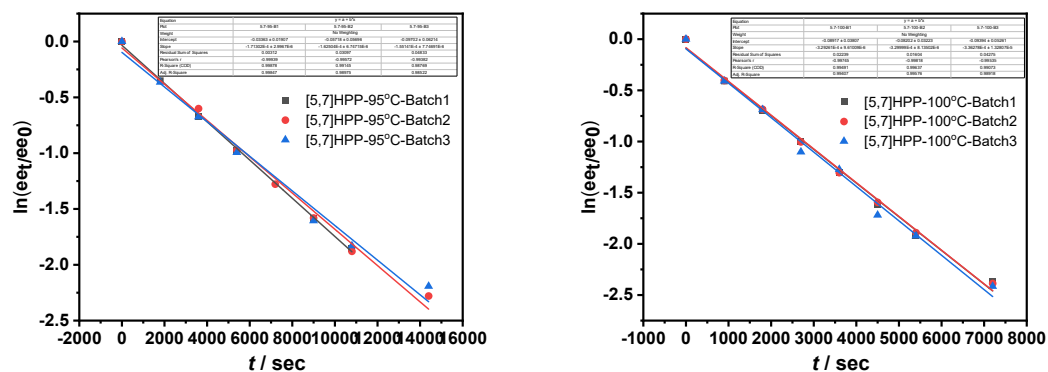


Figure A5.18. First order decay plots from three independent measurements for [5,7]HPP at 95°C (left) and 100°C (right).

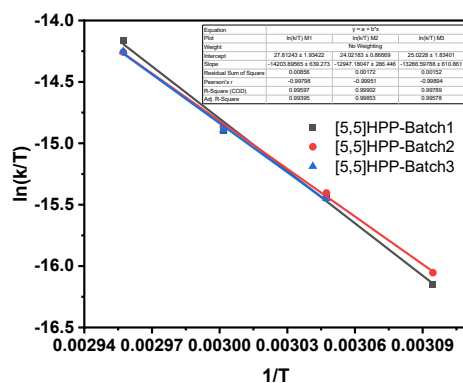


Figure A5.19. Eyring plot for [5,5]HPP.

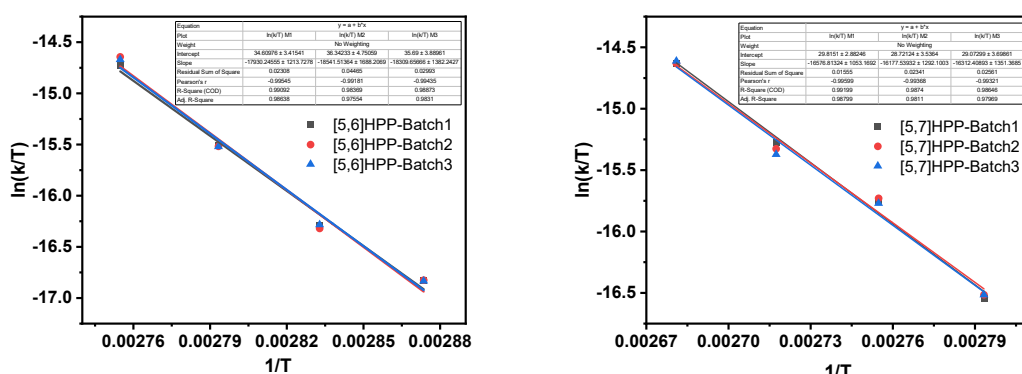


Figure A5.20. Eyring plot for [5,6]HPP and [5,7]HPP.

Table A5.1: Thermodynamic data [5,5]HPP (enthalpy  $\Delta F_{en}^\ddagger$  and entropy  $\Delta S_{en}^\ddagger$ ).

	Slope	Intercept	$\Delta H^\ddagger$ (kcal/mol)	$\Delta S^\ddagger$ (cal/molK)	$\Delta H_{avg}^\ddagger$ (kcal/mol)	$\Delta S_{avg}^\ddagger$ (cal/molK)
Batch 1	-14203.90	27.81	28.2	8.0	$26.8 \pm 2.62$	$3.7 \pm 7.92$
Batch 2	-12947.18	24.02	25.7	0.5		
Batch 3	-13286.60	25.02	26.4	2.5		

**Table A5.2:** Activation barriers,  $\Delta G_{en}^\ddagger$  for [5,5]HPP.

T (kelvin)	Batch 1	Batch 2	Batch 3	$\Delta G^\ddagger$ (kcal/mol)
323	25.6	25.6	25.6	$25.6 \pm 0.06$
328	25.6	25.5	25.6	$25.6 \pm 0.03$
333	25.5	25.5	25.6	$25.5 \pm 0.02$
338	25.5	25.5	25.5	$25.5 \pm 0.06$

**Table A5.3:** Thermodynamic data [5,6]HPP (enthalpy  $\Delta H_{en}^\ddagger$  and entropy  $\Delta S_{en}^\ddagger$ ).

	Slope	Intercept	$\Delta H^\ddagger$ (kcal/mol)	$\Delta S^\ddagger$ (cal/molK)	$\Delta H_{avg}^\ddagger$ (kcal/mol)	$\Delta S_{avg}^\ddagger$ (cal/molK)
Batch 1	-17930.24	34.61	35.6	21.6	$36.3 \pm 1.24$	$23.4 \pm 3.48$
Batch 2	-18541.51	36.34	36.8	25.0		
Batch 3	-18309.65	35.70	36.4	23.7		

**Table A5.4:** Activation barriers,  $\Delta G_{en}^\ddagger$  for [5,6]HPP.

T (kelvin)	Batch 1	Batch 2	Batch 3	$\Delta G^\ddagger$ (kcal/mol)
348.15	28.1	28.1	28.1	$28.1 \pm 0.03$
353.15	28.0	28.0	28.0	$28.0 \pm 0.01$
358.15	27.9	27.9	27.9	$27.9 \pm 0.0$
363.15	27.8	27.8	27.7	$27.8 \pm 0.02$

**Table A5.5:** Thermodynamic data [5,7]HPP (enthalpy  $\Delta H_{en}^\ddagger$  and entropy  $\Delta S_{en}^\ddagger$ ).

	Slope	Intercept	$\Delta H^\ddagger$ (kcal/mol)	$\Delta S^\ddagger$ (cal/molK)	$\Delta H^\ddagger$ (kcal/mol)	$\Delta S^\ddagger$ (cal/molK)
Batch 1	-16576.81	29.81	32.9	12.0	$32.5 \pm 0.82$	$10.8 \pm 2.25$
Batch 2	-16177.54	28.72	32.1	9.9		
Batch 3	-16312.40	29.07	32.4	10.6		

**Table A5.6:** Activation barriers,  $\Delta G_{en}^\ddagger$  for [5,7]HPP.

T (kelvin)	Batch 1	Batch 2	Batch 3	$\Delta G^\ddagger$ (kcal/mol)
358	28.6	28.6	28.6	$28.6 \pm 0.02$
363	28.6	28.6	28.6	$28.6 \pm 0.01$
368	28.5	28.5	28.5	$28.5 \pm 0.02$
373	28.5	28.5	28.5	$28.5 \pm 0.02$

## Optical and Chiroptical Properties

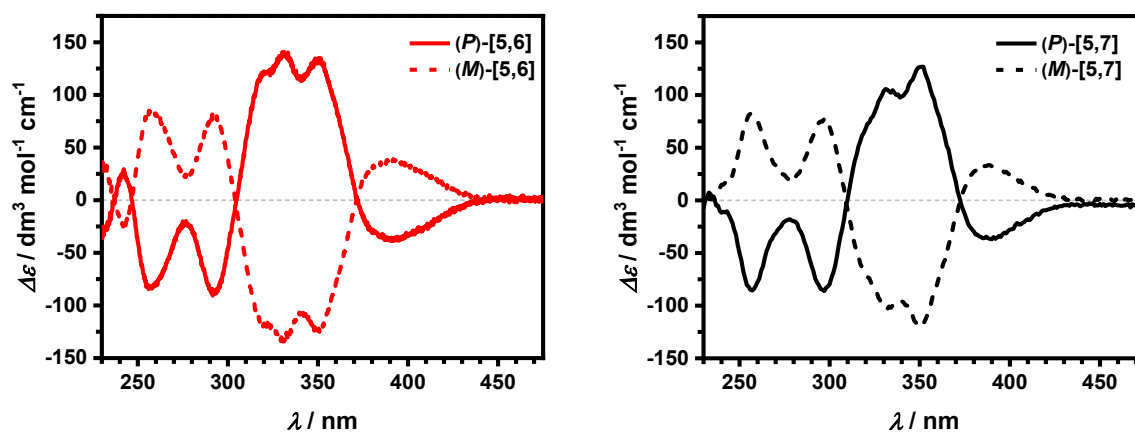


Figure A5.21. Circular dichroism spectra of [5,6]HPP and [5,7]HPP.

**DFT Calculations:** All calculations were performed with Gaussian 09<sup>40</sup> (release D.01) or Gaussian 16<sup>41</sup> (release C.02) software. Geometries of molecules were optimized at D3-B3LYP/6-31g(d) level of theory. The character of stationary points on potential energy surface was determined by subsequent frequency calculations. For transition states, IRC calculations were performed, accompanied by the full geometry optimization at the end of the IRC path, to find the conformers that are connected via the optimized transition states. The default UltraFine integration grid was used in all calculations.

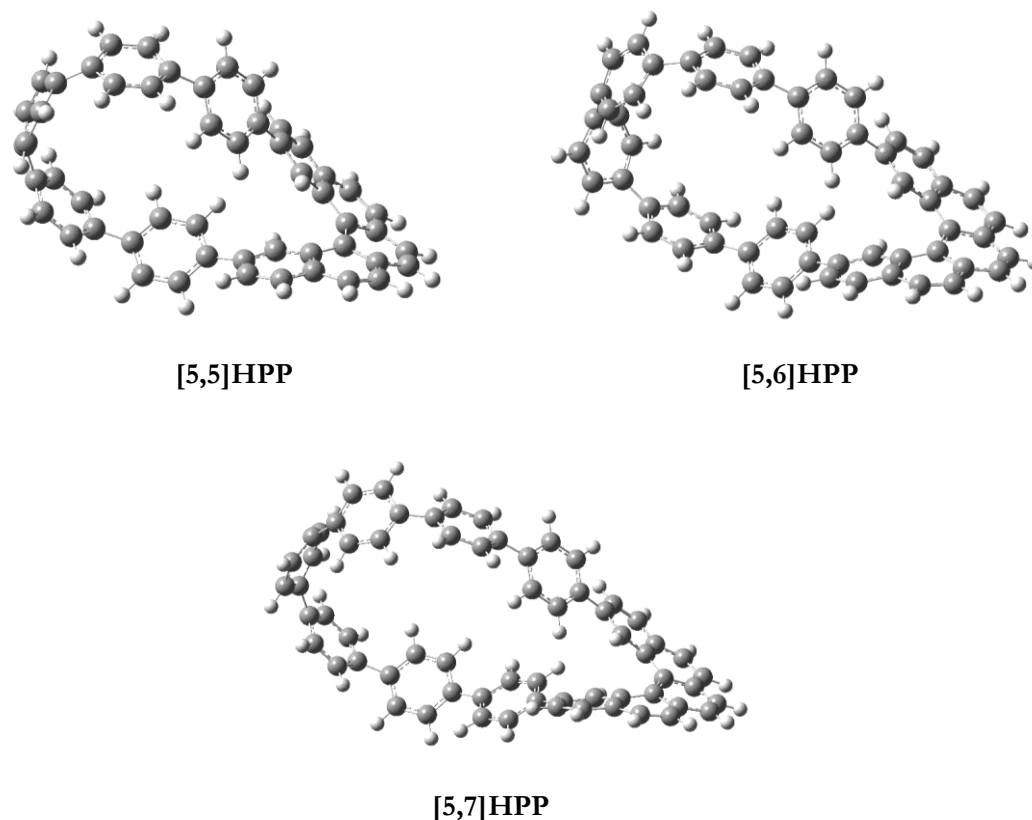
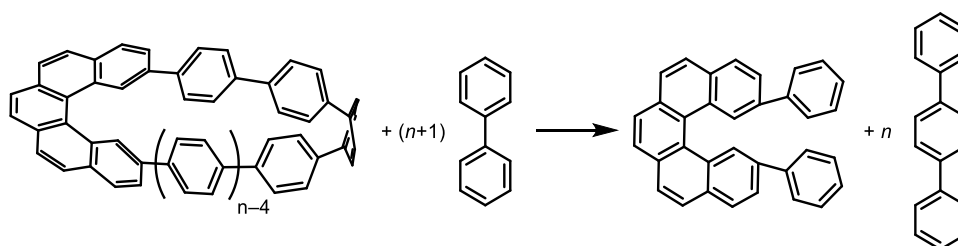


Figure A5.22. The lowest energy conformation identified for [5,*m*]HPPs (*m* = 5–7) at the B3LYP-D3/cc-pVTZ level of theory on B3LYP-D3/6-31G(d) geometries.

A conformational search for [5,6]HPP and [5,7]HPP was performed using Avogadro software<sup>42</sup> at MMFF94 level of theory. A set of low energy conformers was identified and then optimized using D3-B3LYP functional with 6-31g(d) basis set. We found 7 and 11 unique conformers for [5,6]HPP and [5,7]HPP, respectively. Only two distinct conformers could be found for [5,5]HPP. The energies of these conformers were then obtained by single point calculations with cc-pVTZ basis set. The lowest energy conformers were then taken as the “ground state” from which the enantiomerization process takes place. The geometries of these three conformers are given in Figure A5.22.

**Strain Energy and Activation Enthalpy Calculations:** Strain energies were estimated via homodesmotic reactions (Scheme A5.1) on the lowest energy conformers of [5,*m*]HPPs (*m* = 5–7). Single point energies calculated on D3-B3LYP/cc-pVTZ level of theory were corrected by unscaled zero-point vibrational energy (ZPVE) correction from D3-B3LYP/6-31g(d). We also used StrainViz software developed by Jasti group<sup>43</sup> to visualize local strain of [5,*m*]HPPs (*m* = 6,7) and estimate total strain energy, which was nearly identical to the strain energy obtained via homodesmotic reactions. In addition, we calculated the strain energies of the [5]helicene fragments in the structure of the [5,*m*]HPPs (*m* = 5–7) lowest energy minima (“ground state”) and in the corresponding transition states of enantiomerization. The fragments were obtained by trimming all parts of the molecule except the [5]helicene unit to which two hydrogen atoms were attached at 2,13-positions to fill the valency. Subsequently, all coordinates were frozen except of the two new hydrogen atoms to preserve the geometries of the fragment that it had in the corresponding structure. After the full optimization of the six Cartesian coordinates of the two hydrogen atoms on the B3LYP-D3/6-31G(d) level of theory, the strain energy was then calculated as the energy difference of the fragment with respect to the fully relaxed [5]helicene energy minimum or the *C<sub>s</sub>* transition state of its enantiomerization. The used energies were obtained by single point energy calculations at the B3LYP-D3/cc-pVTZ level of theory.



Scheme A5.1.

**Table A5.7.** Thermochemistry for the homodesmotic reactions shown in Scheme A5.1. The B3LYP-D3/cc-pVTZ electronic energies and their corrections by adding the zero-point vibrational energies (ZPVEs) are listed.

Molecule	ZPVE / Hartree	$E_{el}$ / Hartree	$E_{corr}$ / Hartree
9,12-diphenyl[5]helicene	0.451325	-1309.411202500	-1308.959877500
biphenyl	0.182137	-463.481180258	-463.299043258
terphenyl	0.263352	-694.624576988	-694.361224988
[5,5]HPP	0.672603	-2001.54576908	-2000.87316608
[5,6]HPP	0.754060	-2232.69951195	-2231.94546295
[5,7]HPP	0.835454	-2463.851801940	-2463.016347940

**Table A5.8.** Calculated strain energies of [5,*m*]HPPs (*m* = 5–7).

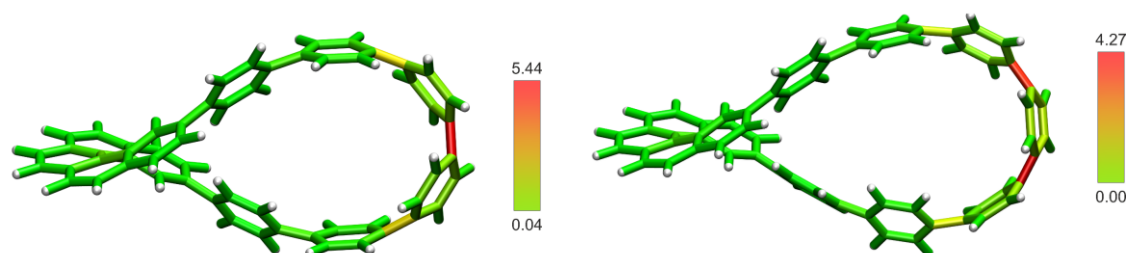
Molecule	Strain Energy <sup>a</sup> / kcal mol <sup>-1</sup>	Strain Energy <sup>b</sup> / kcal mol <sup>-1</sup>
[5,5]HPP	61.9	n.a. <sup>c</sup>
[5,6]HPP	55.5	55.1
[5,7]HPP	50.0	50.4

<sup>a</sup>Strain energy obtained via homodesmotic reaction (Scheme A5.1) and B3LYP method (see Table A5.7). <sup>b</sup>Strain energy obtained via StrainViz. <sup>c</sup>Not available.

**Table A5.9.** Calculated strain energies of [5]helicene fragments in the energy minima and transition states of 2,13-diphenyl-[5]helicene and [5,*m*]HPPs (*m* = 5–7).

Molecule	Geometry	Strain Energy <sup>a</sup> / kcal mol <sup>-1</sup>
2,13-diphenyl-[5]helicene	energy minimum	0.9
	transition state	0.6
[5,5]HPP	energy minimum	1.1
	transition state	3.5
[5,6]HPP	energy minimum	0.9
	transition state	2.6
[5,7]HPP	energy minimum	0.9
	transition state	2.2

<sup>a</sup>Strain energy obtained as the energy difference of the fully relaxed [5]helicene in its lowest energy minimum or the enantiomerization transition state and the energy of the [5]helicene fragment from the corresponding energy minima or transition states of [5,*m*]HPPs (*m* = 5–7). Using B3LYP method (see Table A5.7).

**Figure A5.23.** Total strain visualization of [5,*m*]HPPs (*m* = 6,7) by StrainViz with energies in kcal mol<sup>-1</sup>.

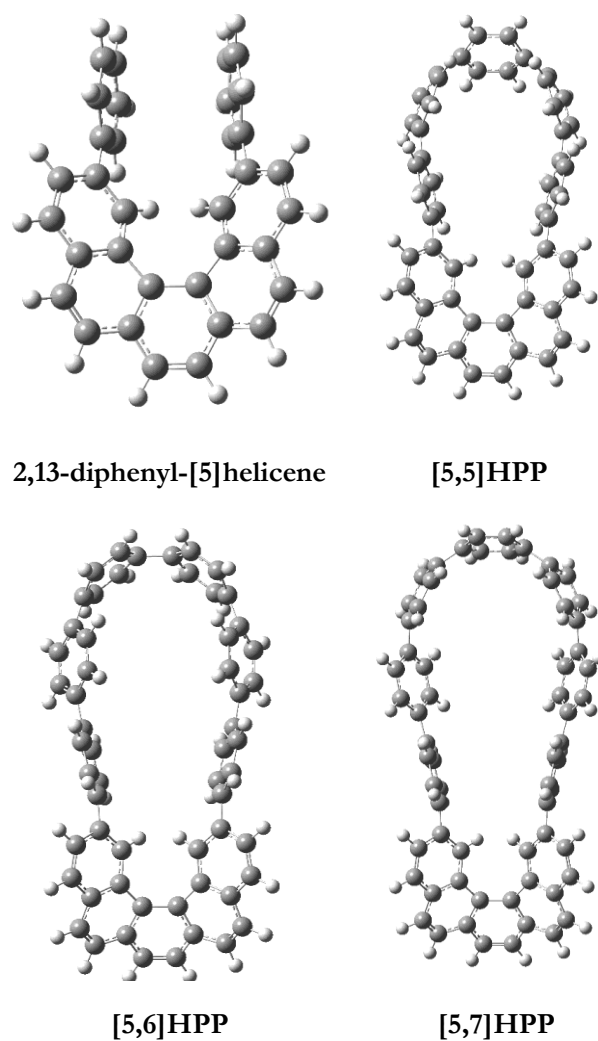


**Figure A5.24.** Transition state geometries of [5,*m*]HPPs (*m* = 5–7) and 2,13-diphenyl-[5]helicene.

**Table A5.10.** Calculated energies of activation<sup>a,b</sup> (at 0K) of enantiomerization of [5]helicene, 2,13-diphenyl-[5]helicene, and [5,*m*]HPPs (*m* = 5–7).

Molecule	$\Delta H^\ddagger$ / kcal mol <sup>-1</sup>				
	B3LYP-D3	wB97XD	M06-2X-D3	MN15	BMK-D3
[5]helicene	23.8	24.6	25.3	24.7	25.1
2,13-diphenyl-[5]helicene	24.9	25.5	26.8	26.2	27.3
<b>[5,5]HPP</b>	25.6	25.9	26.5	26.2	27.2
<b>[5,6]HPP</b>	28.0	29.3	29.7	29.4	30.1
<b>[5,7]HPP</b>	29.2	29.9	30.6	30.6	31.3
<b>[5,8]HPP</b>	30.1	31.1	31.8	31.6	33.0

<sup>a</sup>The enthalpy correction to 298 K decreases the barriers by 0.3–0.4 kcal mol<sup>-1</sup> for all transition states. <sup>b</sup>With cc-pVTZ basis set on B3LYP-D3/6-31G(d) geometries; energies involve unscaled ZPVE correction.

**Table A5.11.** Calculated geometry parameters<sup>a</sup>  $d_{1-14}$  and  $\theta$  in the energy minima of [5]helicene, 2,13-diphenyl-[5]helicene, and [5,*m*]HPPs ( $m = 5-7$ ).

Molecule	$d_{1-14}$ / Å	$\theta$ / °
[5]helicene	2.949	22.06
2,13-diphenyl-[5]helicene	2.914	22.24
<b>[5,5]HPP</b>	3.035	22.76
<b>[5,6]HPP</b>	2.999	22.9
<b>[5,7]HPP</b>	2.946	22.58

<sup>a</sup>Parameters are defined according to ref<sup>8</sup>. Briefly,  $d_{1-14}$  is the C1–C14 distance in Å and the twist angle  $\theta$  is calculated as an average value of torsional angles of all phenanthrene subunits of [5]helicene fragments in individual compounds.

**Table A5.12.** Calculated entropies (in cal mol<sup>-1</sup> K<sup>-1</sup>) of [5]helicene, 2,13-diphenyl-[5]helicene, [5,*m*]HPPs ( $m = 5-7$ ), and their transition states of enantiomerization.

Molecule	Energy minimum	Transition state	Enantiomerization	$\Delta S^\ddagger$ (kcal mol <sup>-1</sup> ), 298.15 K
[5]helicene	117.8	116.7	-1.1	-0.3
2,13-diphenyl-[5]helicene	164.5	162.4	-2.1	-0.6
<b>[5,5]HPP</b>	219.1	212.7	-6.4	-1.9
<b>[5,6]HPP</b>	237.1	236.4	-0.7	-0.2
<b>[5,7]HPP</b>	260.8	258.8	-2.0	-0.6

<sup>a</sup>Parameters are defined according to ref<sup>8</sup>. Briefly,  $d_{1-14}$  is the C1–C14 distance in Å and the twist angle  $\theta$  is calculated as an average value of torsional angles of all phenanthrene subunits of [5]helicene fragments in individual compounds.

## 5.5 References

- (1) Gingras, M. One Hundred Years of Helicene Chemistry. Part 1: Non-Stereoselective Syntheses of Carbohelicenes. *Chem. Soc. Rev.* **2013**, *42* (3), 968–1006. <https://doi.org/10.1039/C2CS35154D>.
- (2) Ravat, P.; Šolomek, T.; Juriček, M. Helicenes as Chiroptical Photoswitches. *ChemPhotoChem* **2019**, *3* (4), 180–186. <https://doi.org/10.1002/cptc.201800229>.
- (3) Gingras, M.; Félix, G.; Peresutti, R. One Hundred Years of Helicene Chemistry. Part 2: Stereoselective Syntheses and Chiral Separations of Carbohelicenes. *Chem. Soc. Rev.* **2013**, *42* (3), 1007–1050. <https://doi.org/10.1039/C2CS35111K>.
- (4) Martin, R. H.; Marchant, M.-J. Thermal Racemisation of [6], [7], [8] and [9] Helicene. *Tetrahedron Lett.* **1972**, *13* (35), 3707–3708. [https://doi.org/10.1016/S0040-4039\(01\)94141-3](https://doi.org/10.1016/S0040-4039(01)94141-3).
- (5) Martin, R. H.; Marchant, M. J. Thermal Racemisation of Hepta-, Octa-, and Nonahelicene: Kinetic Results, Reaction Path and Experimental Proofs That the Racemisation of Hexa- and Heptahelicene Does Not Involve an Intramolecular Double Diels–Alder Reaction. *Tetrahedron* **1974**, *30* (2), 347–349. [https://doi.org/10.1016/S0040-4020\(01\)91469-3](https://doi.org/10.1016/S0040-4020(01)91469-3).
- (6) Lindner, H. J. Atomisierungsenergien Gespannter Konjugierter Kohlenwasserstoffe—I: Razemisierungsenergien von Helicenen. *Tetrahedron* **1975**, *31* (3), 281–284. [https://doi.org/10.1016/0040-4020\(75\)85081-2](https://doi.org/10.1016/0040-4020(75)85081-2).
- (7) Ravat, P. Carbo[n]Helicenes Restricted to Enantiomerize: An Insight into the Design Process of Configurationally Stable Functional Chiral PAHs. *Chem. – Eur. J.* **2021**, *27* (12), 3957–3967. <https://doi.org/10.1002/chem.202004488>.
- (8) Ravat, P.; Hinkelmann, R.; Steinebrunner, D.; Prescimone, A.; Bodoky, I.; Juriček, M. Configurational Stability of [5]Helicenes. *Org. Lett.* **2017**, *19* (14), 3707–3710. <https://doi.org/10.1021/acs.orglett.7b01461>.
- (9) Newman, M. S.; Lednicer, D. The Synthesis and Resolution of Hexahelicene. *J. Am. Chem. Soc.* **1956**, *78* (18), 4765–4770. <https://doi.org/10.1021/ja01599a060>.

- (10) Barroso, J.; Cabellos, J. L.; Pan, S.; Murillo, F.; Zarate, X.; Fernandez-Herrera, M. A.; Merino, G. Revisiting the Racemization Mechanism of Helicenes. *Chem. Commun.* **2017**, *54* (2), 188–191. <https://doi.org/10.1039/C7CC08191J>.
- (11) Goedicke, Ch.; Stegemeyer, H. Resolution and Racemization of Pentahelicene. *Tetrahedron Lett.* **1970**, *11* (12), 937–940. [https://doi.org/10.1016/S0040-4039\(01\)97871-2](https://doi.org/10.1016/S0040-4039(01)97871-2).
- (12) Robert, A.; Naulet, G.; Bock, H.; Vanthuynne, N.; Jean, M.; Giorgi, M.; Carissan, Y.; Aroulanda, C.; Scalabre, A.; Pouget, E.; Duroola, F.; Coquerel, Y. Cyclobishelicenes: Shape-Persistent Figure-Eight Aromatic Molecules with Promising Chiroptical Properties. *Chem. – Eur. J.* **2019**, *25* (63), 14364–14369. <https://doi.org/10.1002/chem.201902637>.
- (13) Zhou, Q.; Hou, X.; Wang, J.; Ni, Y.; Fan, W.; Li, Z.; Wei, X.; Li, K.; Yuan, W.; Xu, Z.; Zhu, M.; Zhao, Y.; Sun, Z.; Wu, J. A Fused [5]Helicene Dimer with a Figure-Eight Topology: Synthesis, Chiral Resolution, and Electronic Properties. *Angew. Chem. Int. Ed.* **2023**, *62* (23), e202302266. <https://doi.org/10.1002/anie.202302266>.
- (14) Thulin, B.; Wennerstrom, O. Propellene or Bi-2,13-Pentahelicenylene. *Acta Chem. Scand., B, Org. Chem. Biochem.*, 1976, *30*, 688–690. <https://doi.org/10.3891/acta.chem.scand.30b-0688>.
- (15) Krzeszewski, M.; Ito, H.; Itami, K. Infinitene: A Helically Twisted Figure-Eight [12]Circulene Topoisomer. *J. Am. Chem. Soc.* **2022**, *144* (2), 862–871. <https://doi.org/10.1021/jacs.1c10807>.
- (16) Fan, W.; Fukunaga, T. M.; Wu, S.; Han, Y.; Zhou, Q.; Wang, J.; Li, Z.; Hou, X.; Wei, H.; Ni, Y.; Isobe, H.; Wu, J. Synthesis and Chiral Resolution of a Triply Twisted Möbius Carbon Nanobelt. *Nat. Synth.* **2023**, *2* (9), 880–887. <https://doi.org/10.1038/s44160-023-00317-3>.
- (17) Malinčík, J.; Gaikwad, S.; Mora-Fuentes, J. P.; Boillat, M.-A.; Prescimone, A.; Häussinger, D.; Campaña, A. G.; Šolomek, T. Circularly Polarized Luminescence in a Möbius Helicene Carbon Nanohoop\*\*. *Angew. Chem. Int. Ed.* **2022**, *61* (37), e202208591. <https://doi.org/10.1002/anie.202208591>.
- (18) Malinčík, J.; Šolomek, T. Topological Bistability of the  $\pi$ -System in a Helicene Carbon Nanohoop. *Synlett* **2024**, *35*, 1739–1744. <https://doi.org/10.1055/a-2223-7245>.
- (19) Kovida, K.; Malinčík, J.; Šolomek, T. Effect of  $\pi$ -Electron Conjugation on the Chiroptical Properties of Helicene Carbon Nanohoos. *Helv. Chim. Acta* **2025**, *108* (4), e202400166. <https://doi.org/10.1002/hlca.202400166>.
- (20) Kovida, K.; Malinčík, J.; M. Cruz, C.; G. Campaña, A.; Šolomek, T. Role of Exciton Delocalization in Chiroptical Properties of Benzothiadiazole Carbon Nanohoos. *Chem. Sci.* **2025**, *16* (3), 1405–1410. <https://doi.org/10.1039/D4SC07333A>.
- (21) Schaub, T. A.; Margraf, J. T.; Zakharov, L.; Reuter, K.; Jasti, R. Strain-Promoted Reactivity of Alkyne-Containing Cycloparaphenylenes. *Angew. Chem. Int. Ed.* **2018**, *57* (50), 16348–16353. <https://doi.org/10.1002/anie.201808611>.
- (22) Kayahara, E.; Qu, R.; Yamago, S. Bromination of Cycloparaphenylenes: Strain-Induced Site-Selective Bis-Addition and Its Application for Late-Stage Functionalization. *Angew. Chem. Int. Ed.* **2017**, *56* (35), 10428–10432. <https://doi.org/10.1002/anie.201704982>.
- (23) Huang, Z.-A.; Chen, C.; Yang, X.-D.; Fan, X.-B.; Zhou, W.; Tung, C.-H.; Wu, L.-Z.; Cong, H. Synthesis of Oligoparaphenylene-Derived Nanohoos Employing an Anthracene Photodimerization–Cycloreversion Strategy. *J. Am. Chem. Soc.* **2016**, *138* (35), 11144–11147. <https://doi.org/10.1021/jacs.6b07673>.
- (24) Kręćjasz, R. B.; Malinčík, J.; Mathew, S.; Štacko, P.; Šolomek, T. Strain-Induced Photochemical Opening of Ferrocene[6]Cycloparaphenylene: Uncaging of Fe<sup>2+</sup> with Green Light. *J. Am. Chem. Soc.* **2025**, *147* (12), 10231–10237. <https://doi.org/10.1021/jacs.4c15818>.
- (25) Hermann, M.; Wassy, D.; Kohn, J.; Seitz, P.; Betschart, M. U.; Grimme, S.; Esser, B. Chiral Dibenzopentalene-Based Conjugated Nanohoos through Stereoselective Synthesis. *Angew. Chem. Int. Ed.* **2021**, *60* (19), 10680–10689. <https://doi.org/10.1002/anie.202016968>.
- (26) Omachi, H.; Segawa, Y.; Itami, K. Synthesis and Racemization Process of Chiral Carbon Nanorings: A Step toward the Chemical Synthesis of Chiral Carbon Nanotubes. *Org. Lett.* **2011**, *13* (9), 2480–2483. <https://doi.org/10.1021/ol200730m>.
- (27) Jhulki, S.; Mishra, A. K.; Chow, T. J.; Moorthy, J. N. Helicenes as All-in-One Organic Materials for Application in OLEDs: Synthesis and Diverse Applications of Carbo- and Aza[5]Helical Diamines. *Chem – Eur J* **2016**, *22* (27), 9375–9386. <https://doi.org/10.1002/chem.201600668>.
- (28) Xia, J.; Bacon, J. W.; Jasti, R. Gram-Scale Synthesis and Crystal Structures of [8]- and [10]CPP, and the Solid-State Structure of C<sub>60</sub>@[10]CPP. *Chem. Sci.* **2012**, *3* (10), 3018. <https://doi.org/10.1039/c2sc20719b>.
- (29) Patel, V. K.; Kayahara, E.; Yamago, S. Practical Synthesis of [n]Cycloparaphenylenes (N=5, 7–12) by H<sub>2</sub>SnCl<sub>4</sub>-Mediated Aromatization of 1,4-Dihydroxycyclo-2,5-Diene Precursors. *Chem. – Eur. J.* **2015**, *21* (15), 5742–5749. <https://doi.org/10.1002/chem.201406650>.
- (30) Sisto, T. J.; Jasti, R. Overcoming Molecular Strain: Synthesis of [7]Cycloparaphenylene. *Synlett* **2012**, *2012*, 483–489. <https://doi.org/10.1055/s-0031-1290360>.
- (31) Darzi, E. R.; White, B. M.; Loventhal, L. K.; Zakharov, L. N.; Jasti, R. An Operationally Simple and Mild Oxidative Homocoupling of Aryl Boronic Esters To Access Conformationally Constrained Macrocycles. *J. Am. Chem. Soc.* **2017**, *139* (8), 3106–3114. <https://doi.org/10.1021/jacs.6b12658>.

- (32) Yang, H.; Guo, S.; Guo, W.; Liu, L.; Liu, X.; He, J.; Fan, Y.; Lian, Z.; Li, X.; Huang, S.; Chen, X.; Wang, Y.; Jiang, H. [5]Helicene-Embedded Cycloparaphenylene Nanohoops with Möbius Topology: Synthesis, Photophysical Properties, and Aromaticity. *Chem. – Asian J.* **2025**, *20* (16), e00205. <https://doi.org/10.1002/asia.202500205>.
- (33) Darzi, E. R.; Jasti, R. The Dynamic, Size-Dependent Properties of [5]–[12]Cycloparaphenylenes. *Chem. Soc. Rev.* **2015**, *44* (18), 6401–6410. <https://doi.org/10.1039/C5CS00143A>.
- (34) Birks, J. B.; Birch, D. J. S.; Cordemans, E.; Vander Donckt, E. Fluorescence of the Higher Helicenes. *Chem. Phys. Lett.* **1976**, *43* (1), 33–36. [https://doi.org/10.1016/0009-2614\(76\)80750-6](https://doi.org/10.1016/0009-2614(76)80750-6).
- (35) Kubo, H.; Hirose, T.; Matsuda, K. Control over the Emission Properties of [5]Helicenes Based on the Symmetry and Energy Levels of Their Molecular Orbitals. *Org. Lett.* **2017**, *19* (7), 1776–1779. <https://doi.org/10.1021/acs.orglett.7b00548>.
- (36) Rickhaus, M.; Jundt, L.; Mayor, M. Determining Inversion Barriers in Atrop- Isomers – A Tutorial for Organic Chemists. *CHIMIA* **2016**, *70* (3), 192–192. <https://doi.org/10.2533/chimia.2016.192>.
- (37) Mannancherry, R.; Šolomek, T.; Cavalli, D.; Malinčík, J.; Häußinger, D.; Prescimone, A.; Mayor, M. Sulfone “Geländer” Helices: Revealing Unexpected Parameters Controlling the Enantiomerization Process. *J. Org. Chem.* **2021**, *86* (8), 5431–5442. <https://doi.org/10.1021/acs.joc.0c03016>.
- (38) Weiland, K. J.; Brandl, T.; Atz, K.; Prescimone, A.; Häußinger, D.; Šolomek, T.; Mayor, M. Mechanical Stabilization of Helical Chirality in a Macrocyclic Oligothiophene. *J. Am. Chem. Soc.* **2019**, *141* (5), 2104–2110. <https://doi.org/10.1021/jacs.8b11797>.
- (39) Sisto, T. J.; Golder, M. R.; Hirst, E. S.; Jasti, R. Selective Synthesis of Strained [7]Cycloparaphenylene: An Orange-Emitting Fluorophore. *J. Am. Chem. Soc.* **2011**, *133* (40), 15800–15802. <https://doi.org/10.1021/ja205606p>.
- (40) Frisch, M. J.; Trucks, G. W.; Schlegel, H. B.; Scuseria, G. E.; Robb, M. A.; Cheeseman, J. R.; Scalmani, G.; Barone, V.; Mennucci, B.; Petersson, G. A.; Nakatsuji, H.; Caricato, M.; Li, X.; Hratchian, H. P.; Izmaylov, A. F.; Bloino, J.; Zheng, G.; Sonnenberg, J. L.; Hada, M.; Ehara, M.; Toyota, K.; Fukuda, R.; Hasegawa, J.; Ishida, M.; Nakajima, T.; Honda, Y.; Kitao, O.; Nakai, H.; Vreven, T.; Montgomery, J. A.; Peralta, J. E.; Ogliaro, F.; Bearpark, M.; Heyd, J. J.; Brothers, E.; Kudin, K. N.; Staroverov, V. N.; Kobayashi, R.; Normand, J.; Raghavachari, K.; Rendell, A.; Burant, J. C.; Iyengar, S. S.; Tomasi, J.; Cossi, M.; Rega, N.; Millam, J. M.; Klene, M.; Knox, J. E.; Cross, J. B.; Bakken, V.; Adamo, C.; Jaramillo, J.; Gomperts, R.; Stratmann, R. E.; Yazyev, O.; Austin, A. J.; Cammi, R.; Pomelli, C.; Ochterski, J. W.; Martin, R. L.; Morokuma, K.; Zakrzewski, V. G.; Voth, G. A.; Salvador, P.; Dannenberg, J. J.; Dapprich, S.; Daniels, A. D.; Farkas, Ö.; Foresman, J. B.; Ortiz, J. V.; Cioslowski, J.; Fox, D. J. *Gaussian 09 Revision D.01*; 2009.
- (41) Frisch, M. J.; Trucks, G. W.; Schlegel, H. B.; Scuseria, G. E.; Robb, M. A.; Cheeseman, J. R.; Scalmani, G.; Barone, V.; Petersson, G. A.; Nakatsuji, H.; Li, X.; Caricato, M.; Marenich, A. V.; Bloino, J.; Janesko, B. G.; Gomperts, R.; Mennucci, B.; Hratchian, H. P.; Ortiz, J. V.; Izmaylov, A. F.; Sonnenberg, J. L.; Williams, Ding, F.; Lipparini, F.; Egidi, F.; Goings, J.; Peng, B.; Petrone, A.; Henderson, T.; Ranasinghe, D.; Zakrzewski, V. G.; Gao, J.; Rega, N.; Zheng, G.; Liang, W.; Hada, M.; Ehara, M.; Toyota, K.; Fukuda, R.; Hasegawa, J.; Ishida, M.; Nakajima, T.; Honda, Y.; Kitao, O.; Nakai, H.; Vreven, T.; Throssell, K.; Montgomery Jr., J. A.; Peralta, J. E.; Ogliaro, F.; Bearpark, M. J.; Heyd, J. J.; Brothers, E. N.; Kudin, K. N.; Staroverov, V. N.; Keith, T. A.; Kobayashi, R.; Normand, J.; Raghavachari, K.; Rendell, A. P.; Burant, J. C.; Iyengar, S. S.; Tomasi, J.; Cossi, M.; Millam, J. M.; Klene, M.; Adamo, C.; Cammi, R.; Ochterski, J. W.; Martin, R. L.; Morokuma, K.; Farkas, O.; Foresman, J. B.; Fox, D. J. *Gaussian 16 Rev. C.02*, 2016.
- (42) Hanwell, M. D.; Curtis, D. E.; Lonie, D. C.; Vandermeersch, T.; Zurek, E.; Hutchison, G. R. Avogadro: An Advanced Semantic Chemical Editor, Visualization, and Analysis Platform. *J. Cheminformatics* **2012**, *4* (1), 17. <https://doi.org/10.1186/1758-2946-4-17>.
- (43) Colwell, C. E.; Price, T. W.; Stauch, T.; Jasti, R. Strain Visualization for Strained Macrocycles. *Chem. Sci.* **2020**, *11* (15), 3923–3930. <https://doi.org/10.1039/D0SC00629G>.

